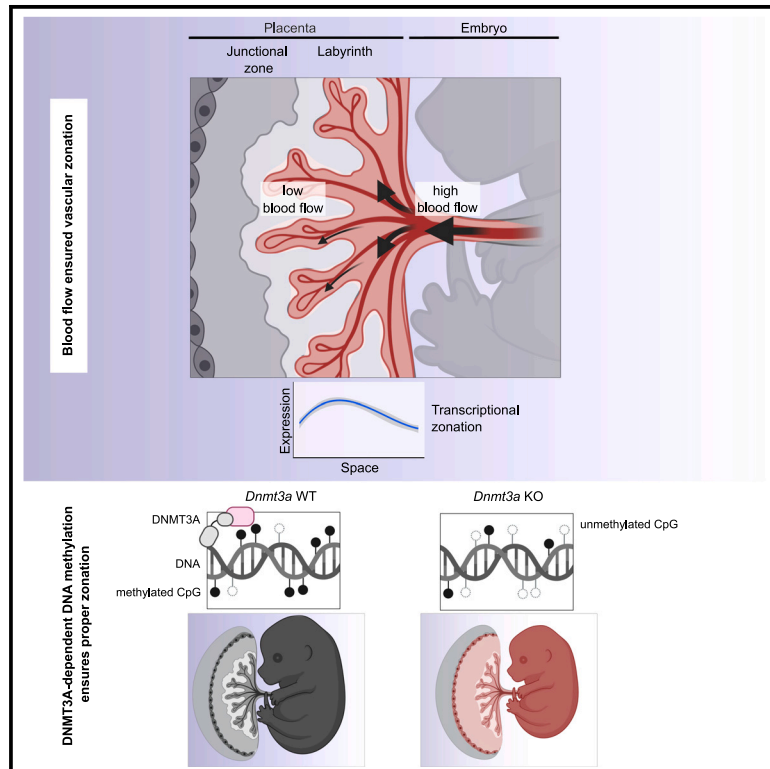# Developmental Cell

The spatial zonation of the murine placental vasculature is specified by epigenetic mechanisms

Graphical abstract

Authors

Stephanie Gehrs, Moritz Jakab,
Ewgenija Gutjahr, ..., Christoph Plass,
Katharina Schlereth,
Hellmut G. Augustin

Correspondence

augustin@angioscience.de (H.G.A.)

In brief

Gehrs et al. demonstrate that the spatial zonation of the murine placental vasculature in the labyrinth is regulated by DNMT3A-dependent DNA methylation. Loss of *Dnmt3a* disrupts vascular-zonated gene expression, impairs angiogenesis, and causes fetal growth retardation, with implications for human placental health and preeclampsia.

Highlights

- The murine labyrinthine placental vasculature is spatially zonated

- Vascular zonation in the murine placenta depends on blood flow

- *Dnmt3a* deficiency impairs placental and postnatal angiogenesis, delaying fetal growth

- *DNMT3A* reduction is associated with preeclampsia in human placental endothelial cells

CellPress

Developmental Cell

Article

The spatial zonation of the murine placental vasculature is specified by epigenetic mechanisms

Stephanie Gehrs,[1,2,3] Moritz Jakab,[1,2] Ewgenija Gutjahr,[4] Zuguang Gu,[5] Dieter Weichenhan,[6] Jan-Philipp Mallm,[7] Carolin Mogler,[8] Matthias Schlesner,[9] Christoph Plass,[6] Katharina Schlereth,[1,2,10,11] and Hellmut G. Augustin[1,2,10,11,12,*]

[1]Division of Vascular Oncology and Metastasis, German Cancer Research Center (DKFZ), 69120 Heidelberg, Germany
[2]European Center for Angioscience (ECAS), Medical Faculty Mannheim, Heidelberg University, 68167 Mannheim, Germany
[3]Faculty of Biosciences, Heidelberg University, 69120 Heidelberg, Germany
[4]Institute of Pathology, University Clinic Heidelberg, 69120 Heidelberg, Germany
[5]Computational Oncology Group, Molecular Precision Oncology Program, National Center for Tumor Diseases (NCT) Heidelberg and German Cancer Research Center (DKFZ), 69120 Heidelberg, Germany
[6]Division of Cancer Epigenomics, German Cancer Research Center (DKFZ), 69120 Heidelberg, Germany
[7]Division of Chromatin Networks, German Cancer Research Center (DKFZ) and Bioquant, 69120 Heidelberg, Germany
[8]Institute of Pathology, TUM School of Medicine, Technical University of Munich, 80333 Munich, Germany
[9]Biomedical Informatics, Data Mining and Data Analytics, Faculty of Applied Computer Science and Medical Faculty, University of Augsburg, 86159 Augsburg, Germany
[10]These authors contributed equally
[11]Senior author
[12]Lead contact
*Correspondence: gehrs.s@googlemail.com (S.G.), augustin@angioscience.de (H.G.A.)
https://doi.org/10.1016/j.devcel.2024.12.037

SUMMARY

The labyrinthian fetoplacental capillary network is vital for proper nourishment of the developing embryo. Dysfunction of the maternal-fetal circulation is a primary cause of placental insufficiency. Here, we show that the spatial zonation of the murine placental labyrinth vasculature is controlled by flow-regulated epigenetic mechanisms. Spatiotemporal transcriptomic profiling identified a gradual change in the expression of epigenetic enzymes, including the *de novo* DNA methyltransferase 3a (DNMT3A). Loss of *Dnmt3a* resulted in DNA hypomethylation and perturbation of zonated placental gene expression. The resulting global DNA hypomethylation impaired the angiogenic capacity of endothelial cells. Global or endothelium-predominant deletion of *Dnmt3a* resulted in impaired placental vascularization and fetal growth retardation (FGR). Human placental endothelial gene expression profiling associated preeclampsia with reduced DNMT3A expression. Collectively, our study identified DMNT3A as critical methylome-regulator of placental endothelial gene expression and function with clinical implications for placental dysfunction, as it occurs during preeclampsia or FGR.

INTRODUCTION

The placenta represents a transient organ at the interface of mother and fetus. It is the source of essential pregnancy-supporting hormones, supplies the developing embryo with nutrients and oxygen, and forms a selective barrier to prevent internal infection.[1] The maternal-fetal interface transports oxygen and nutrients from the maternal bloodstream to the complex branched fetoplacental capillary network representing the functional unit of the placenta. Based on morphological and functional similarity, the human chorionic villi and the mouse labyrinth represent analogous structures.[2,3] Abnormal placental development affects the placental architecture and impairs placental function, resulting in impaired fetal growth. Abnormalities in trophoblast and endothelial cells (ECs) are often implicated in placental insufficiencies.[4,5] Given the pivotal role of the

maternal-fetal circulation for fetal nourishment, its dysregulation has emerged as one of the main pathophysiological features of placental insufficiency. In fact, abnormal growth of the fetoplacental endothelium is the underlying cause of fetal growth retardation (FGR).[6] Similarly, multiple studies have established that a compromised placental circulation and dysregulation of angiogenic molecules represent common features of preeclampsia (PE) and intrauterine growth retardation (IUGR; syn. FGR).[7] Yet, the underlying mechanisms responsible for dysfunctional placental circulation remain largely elusive.

DNA methylation alterations in the placenta have been implicated in the pathogenesis of severe placental disorders.[8–11] In mammalian somatic cells, about 80% of the DNA is methylated, predominantly at cytosines of CpG dinucleotides.[12] The levels of DNA methylation vary during development, starting with a wave of DNA demethylation after fertilization, followed by *de novo*
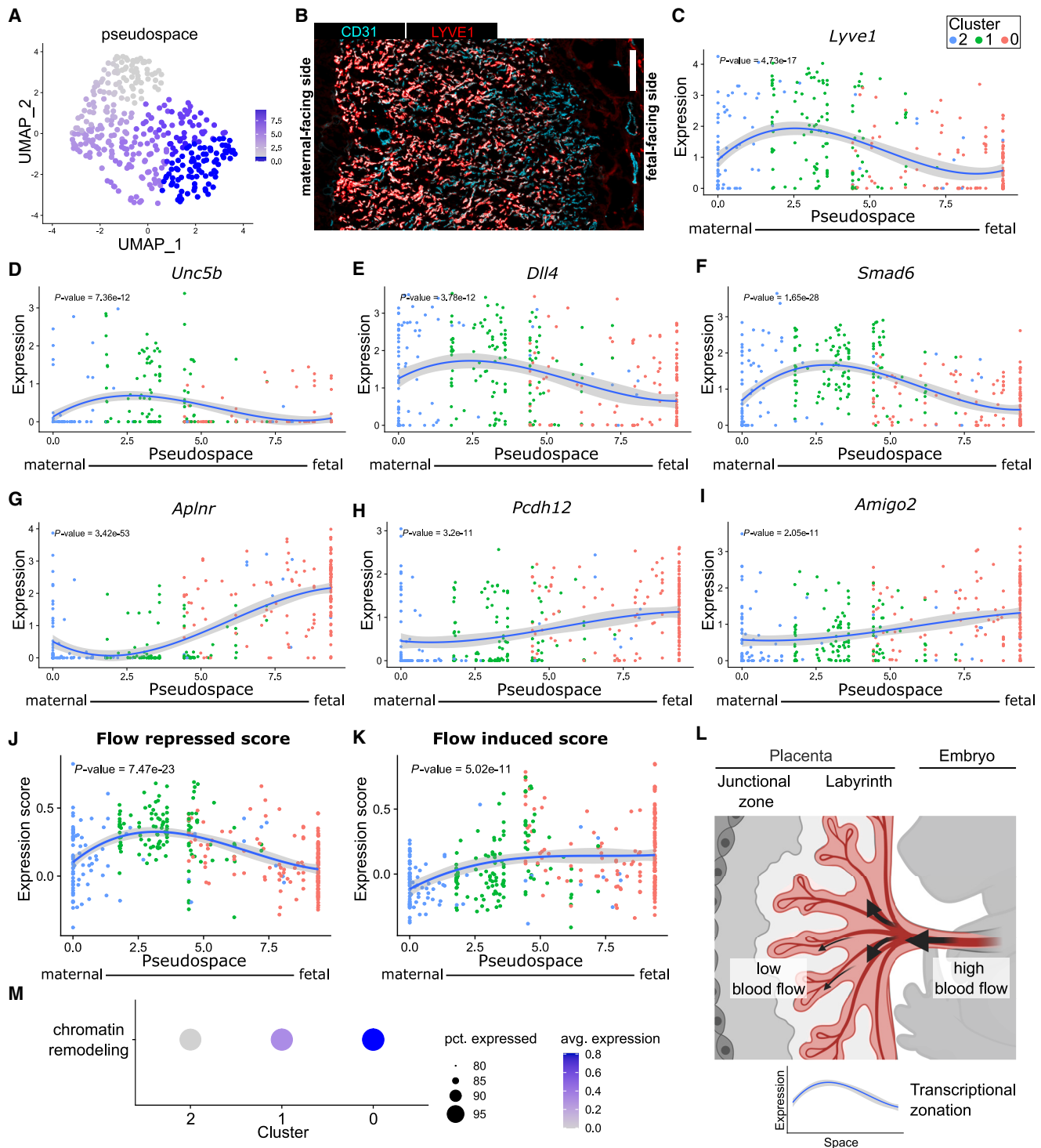
Figure 1. Spatial zonation of the labyrinth placental vasculature

(A) UMAP of labyrinth placenta ECs showing the calculated pseudospace.

(B) Representative image of an E16.5 placenta labyrinth section stained for CD31 and LYVE1. The left side of the image is facing the maternal side (decidua) and the right side of the image is facing toward the fetus. Scale bar: 200μm.

(C) Expression of *Lyve1* in pseudospace.

(D) Expression of *Unc5b* in pseudospace.

(E) Expression of *Dll4* in pseudospace.

(F) Expression of *Smad6* in pseudospace.

Developmental Cell
Article

CellPress
OPEN ACCESS

methylation after zygote implantation.[13] Following implantation of the embryo, DNA methylation patterns are established by *de novo* DNA methyltransferases (DNMTs) 3A and 3B, both of which are highly expressed in the developing embryo. Although DNA methylation levels in the embryo are rapidly re-established, the trophectoderm remains hypomethylated.[14] The global hypomethylation observed, approximately 25% less DNA methylation in human chorionic villi compared with fetal tissue,[15] might be attributed to reduced DNMT1 expression in extra-embryonic tissues.[16] Consequently, this may lead to a diminished capacity for maintaining DNA methylation levels during rapid cell growth.[17] The importance of *de novo* DNA methylation during development was shown in genetic loss-of-function studies in mice, revealing prominent growth impairment and developmental defects.[18] Investigations into the impact of DNA methylation mediated by DNMTs and its subsequent implications on gene regulation have revealed the essential role of DNMT3B in establishing the methylome within the extra-embryonic ectoderm, comprising trophoblast cells.[19] Notably, DNMT3A appeared dispensable for orchestrating methylation patterns within the extra-embryonic ectoderm.[19]

Within the globally methylated mammalian genome, short regions with a high frequency of CpG dinucleotides, called CpG islands (CGIs), remain unmethylated[20] and localize in regulatory elements.[21] Early studies associated DNA methylation with transcriptional repression of CGI-associated genes and transposons, as well as X chromosome inactivation.[22] Genome-wide studies of DNA methylation and individual post-translational modifications of the histone tail have revealed their intimate interplay in a sometimes counterintuitive function in gene regulation. Consequently, the effect of methylation on transcription is context dependent.

Although global DNA hypermethylation in the placenta is associated with being born large for gestational age, specific hypomethylation patterns are observed in IUGR placentas.[11,23] Recent studies link DNMT3A to placental insufficiency. For instance, downregulation of DNMT3A in preeclamptic patients has been associated with reduced migration capacity of trophoblasts.[24] Most of these studies focus on epigenetic changes in trophoblast cells. Yet, it has also been shown that a reduction of DNMT3A can be specifically detected in the fetal capillaries of the chorionic villi of placentas from early growth arrest cases.[25] These findings demonstrate that abnormal placentation is linked to dysregulation of DNA methylation. Considering the functional importance of the fetoplacental capillary network for fetal nourishment and the clinical relevance of DNA methylation, we therefore hypothesized that DNMT3A might act as a critical regulator of the methylome during vascularization of the placenta. This study was consequently aimed at assessing the

role of DNA methylation modifiers in the fetal-derived placenta endothelium.

RESULTS

A flow-dependent spatial zonation of the murine placental vasculature

To molecularly dissect the spatial gene expression changes of the murine placental vasculature, we performed single-cell RNA sequencing (RNA-seq) on labyrinth ECs dissected from four litter-matched embryonic day (E)16.5 placentas (Figure S1A). To this end, we isolated ECs from the labyrinth compartment of the placenta to selectively analyze the fetal-derived endothelium. The sorting strategy proved effective for EC isolation as evidenced by ubiquitous *Pecam1* (also known as *Cd31*) and *Cdh5* expression (Figures S1B and S1C). Low-resolution clustering resulted in a homogeneous capillary EC pool (Figure S1D), which showed a gradual change in gene expression (Figure S1E). As a gradual gene expression pattern is characteristic of essentially all vascular beds,[26] we aimed to generate an insightful trajectory based on pseudospatial clustering.[27] This analysis resulted in a pseudospatial gradient (Figure 1A), in which ECs, identified as clusters 1 and 2 (Figure S1D), reside toward the maternal-facing side of the placenta labyrinth, as shown by LYVE1 and CD31 co-staining on E16.5 placentas (Figure 1B) and *Lyve1* expression in pseudospace (Figure 1C).

Beyond expressing *Lyve1*, ECs at the maternal-facing side expressed elevated levels of genes associated with low blood flow or flow-mediated barrier function, such as *Unc5b*, *Dll4*, and *Smad6* (Figures 1D–1F), suggesting a flow-regulated barrier in this zone of the placenta.[28–31] Conversely, candidate genes known to be upregulated by high blood flow,[30,32,33] such as *Aplnr*, *Pcdh12*, and *Amigo2* were upregulated at the fetal-facing side (Figures 1G–1I). The flow-dependent spatial zonation was further confirmed by an assigned expression score of genes that were either induced or repressed upon the applied flow.[34–37] This analysis unambiguously confirmed (1) an elevated flow-repressed expression score toward the maternal-facing side (Figure 1J) and (2) an elevated flow-induced expression score toward the fetal-facing side (Figures 1K and 1L).

To determine whether the observed spatial transcriptome pattern was indeed flow-mediated, human umbilical vein endothelial cells (HUVECs) were cultured under static and flow conditions (Figure S1F). Model validation experiments were performed by assessing the flow-responsive genes *ANGPT2* and *KLF2* (Figures S1G and S1H). These cellular experiments confirmed that *LYVE1*, *SMAD6*, *DLL4*, and *UNC5B* expression levels were higher under static conditions compared with high flow

(G) Expression of *Aplnr* in pseudospace.

(H) Expression of *Pcdh12* in pseudospace.

(I) Expression of *Amigo2* in pseudospace.

(J) Expression score of flow-repressed genes in pseudospace.

(K) Expression score of flow-induced genes in pseudospace.

(L) Schematic overview showing the murine placenta (left) and the connected embryo (right). The detected transcriptional zonation in space is indicated on the bottom.

(M) Scored expression of genes involved in chromatin remodeling in each placenta EC cluster are shown. Pct. expression refers to the percentage of cells in a cluster expressing the assigned score and avg. expression refers to the average expression level. Individual cells are colored based on their initially associated cell cluster (see Figure S1D). *p*-value of the fitted polynomial regression is shown and the shaded area indicates the 95% confidence interval (C–K).
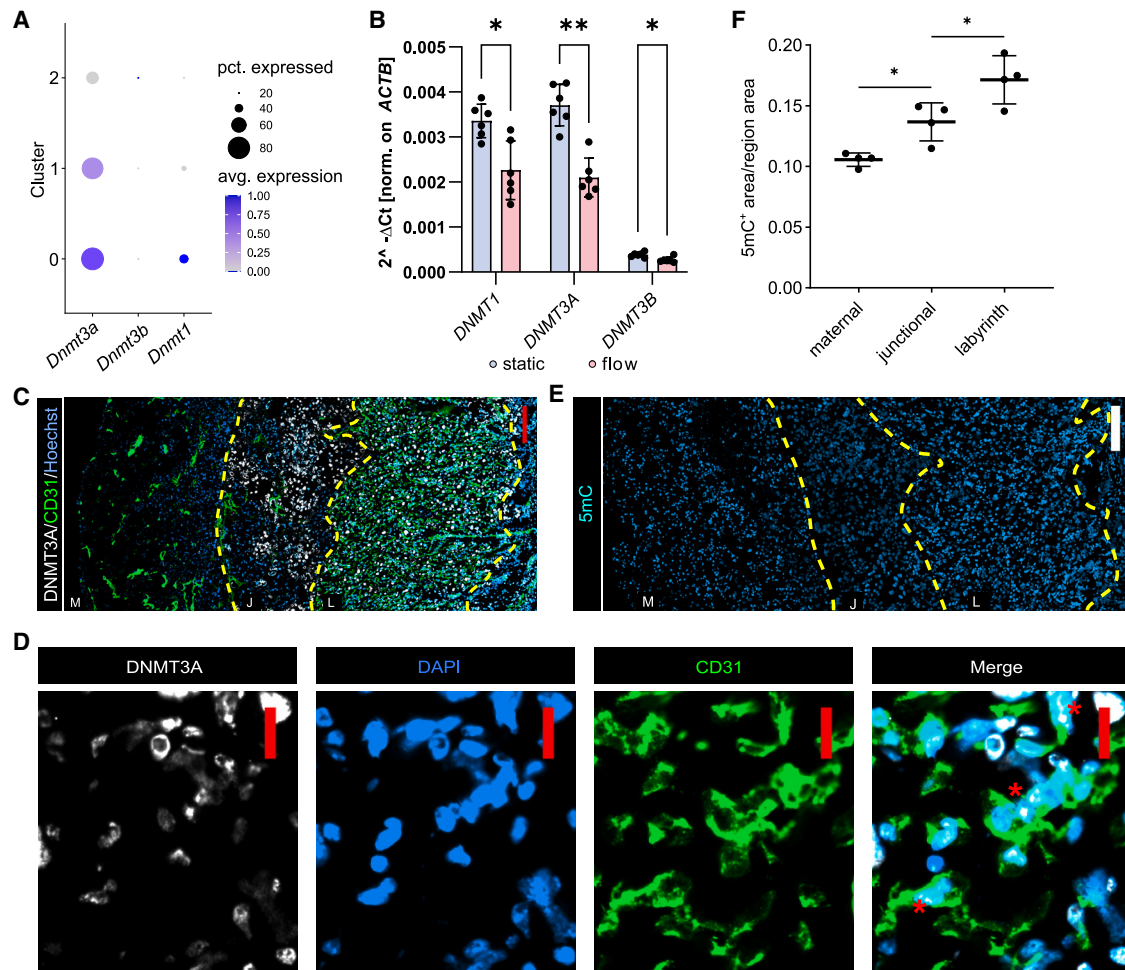
Developmental Cell
Article

Figure 2. *Dnmt3a* is regulated upon blood flow

(A) Dot plot showing the expression of *Dnmts* in the identified placenta labyrinth EC clusters. Pct. expression refers to the percentage of cells in a cluster expressing the shown gene and avg. expression refers to the average expression level.

(B) Relative expression of *DNMT1*, *DNMT3A*, and *DNMT3B* normalized to *ACTB* in HUVECs under static or flow conditions. *n* = 6.

(C) Co-staining of DNMT3A, CD31 (EC marker), and Hoechst (nuclear marker) in the mature murine E16.5 placenta. Placental zones are separated by yellow dashed lines. M, maternal; J, junctional; L, labyrinth compartment. The region situated on the far right corresponds to the chorionic plate. Scale bar: 200 μm.

(D) Zoom-in region of the labyrinth compartment shown in (C). DNMT3A/CD31 double-positive cells are indicated with a red star. Scale bar: 20 μm.

(E) Representative image of 5-methylcytosine (5mC) staining in E14.5 placenta tissue. Placental zones are separated by yellow dashed lines. M, maternal; J, junctional; L, labyrinth compartment. The region situated on the far right corresponds to the chorionic plate. Scale bar: 200 μm.

(F) Quantification of 5mC intensity in different placental regions. *n* = 4. Shown are mean ± SD. The statistical significance was assessed by Mann-Whitney test (B and E). *p < 0.05, **p < 0.01.

(Figure S1I), as observed within the spatial-zonated placental endothelium. Conversely, the expression of *APLNR*, *AMIGO2*, and *PTGS1* was significantly induced under flow conditions (Figure S1J).

In summary, the detailed spatial analysis of EC gene expression of the mature mouse placenta identified a blood flow-dependent, zonated expression pattern in the labyrinth placenta vasculature. In searching for potential mechanisms involved in controlling this spatial-zonated EC transcriptome, we observed an enriched expression score of genes associated with chromatin remodeling (GO: 0006338) in capillary clusters facing the maternal side (Figure 1M), suggesting that epigenetic remodeling in the zonated vasculature may be involved in defining the zonated EC transcriptome.

DNMT3A is the main DNMT expressed in the fetal labyrinth

DNA methylation has been described to play a functional role in nuanced gene expression.[38] Therefore, we analyzed the expression pattern of DNMTs in pseudospace. This analysis revealed that *Dnmt3a* showed the highest expression compared with other DNMTs and was enriched in the fetal-facing and intermediate EC clusters (clusters 0 and 1) (Figure 2A). The flow-dependent expression of *DNMT3A* was additionally confirmed in cellular HUVEC flow experiments (Figures 2B and S1F). Notably, as the expression of *Dnmt1* was restricted to placental development and cell proliferation (Figures S2A and S2B), the persistent expression of *Dnmt3a* suggested a possible functional involvement in the regulation of placental maturation (Figure S2A). In
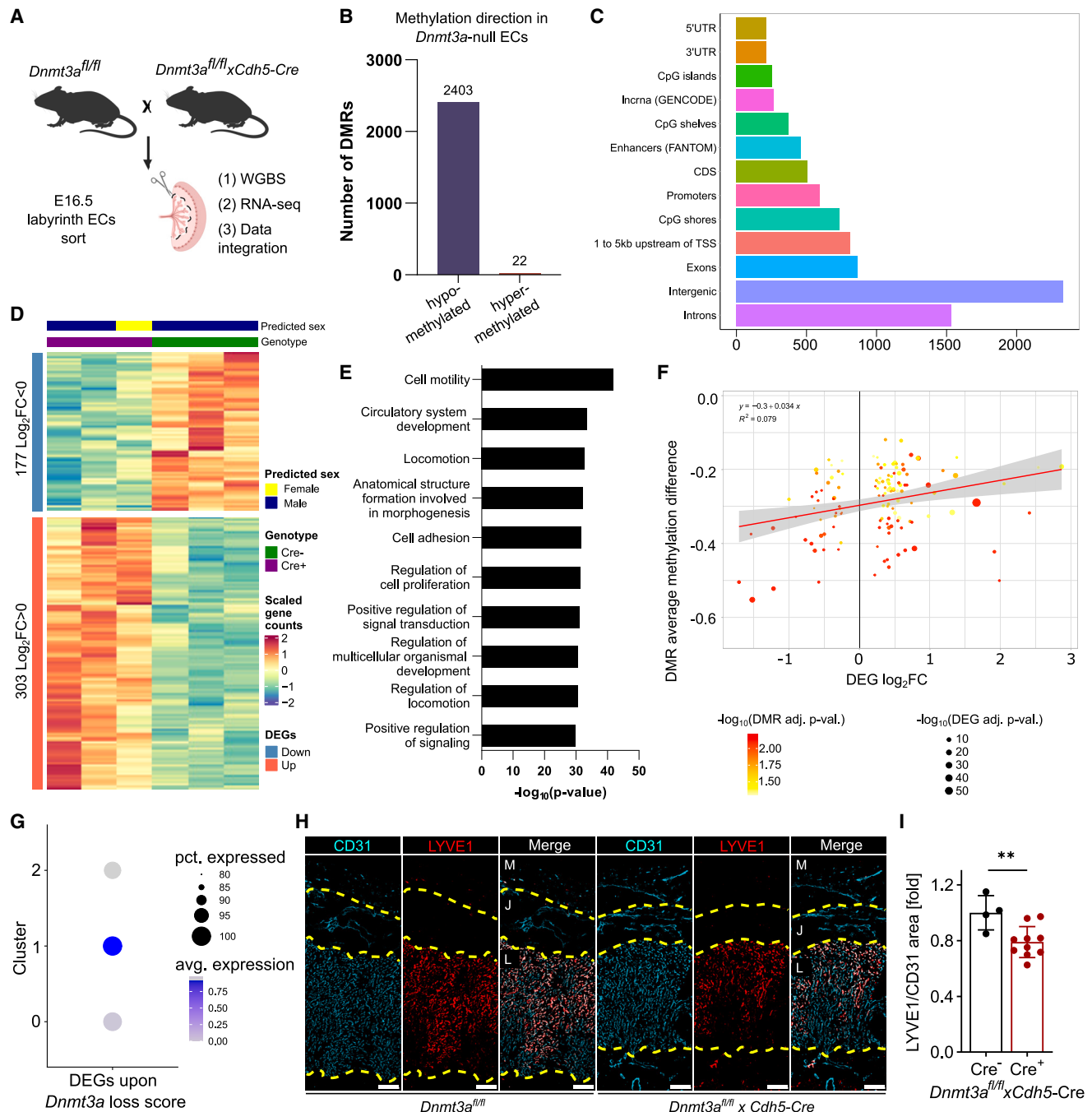
Developmental Cell
Article

CellPress
OPEN ACCESS

Figure 3. DNA hypomethylation in placenta ECs upon *Dnmt3a* loss results in gene deregulation

(A) Breeding scheme showing the generation of litter-matched endothelial-predominant *Dnmt3a*-null embryos. At E16.5, the placenta labyrinth was dissected and ECs were isolated by FACS-sorting. Sorted ECs were further used for (1) whole genome bisulfite sequencing (WGBS) and (2) RNA-seq. Then, data integration was performed (3).

(B) Number of identified DMRs in *Dnmt3a*-null ECs.

(C) Number of DMRs annotated to genomic features.

(D) Heatmap showing the DEGs in ECs isolated from *Dnmt3a^{fl/fl}* (Cre⁻) and *Dnmt3a^{fl/fl}×Cdh5-Cre* (Cre⁺) placentas.

(E) Gene Ontology analysis of DEGs using biological processes.

(F) Association of identified DMRs in DEGs. The average methylation difference of the DMR is displayed on the y axis. The log$_2$FC is displayed on the x axis. The dot size is directly proportional to significance of the DEG ($-\log_{10}$ of the adj. *p* value) and colored by significance of the DMR ($-\log_{10}$ of the adj. *p* value). The shaded area indicates the 95% confidence interval.

(G) Dot plot showing the expression score of DEGs upon *Dnmt3a* loss in labyrinth placenta clusters. Pct. expression refers to the percentage of cells in a cluster expressing the assigned score and avg. expression refers to the average expression level.

line with the prominent expression of *Dnmt3a* in labyrinth ECs, we detected DNMT3A at the protein level in the fetal-derived placental zones (labyrinth and junctional zone) (Figures 2C and 2D). Of note, DNMT3A was not detected in the maternal-derived decidua (Figure 2C). To further assess this differential expression pattern, we split published single-nuclei RNA-seq data of mouse placenta tissue[39] into maternal and fetal ECs (Figures S2C and S2D). This comparative analysis revealed an elevated expression score of genes involved in the writing of DNA methylation marks in fetal vs. maternal ECs (Figure S2E). Notably, *Dnmt3a* was stronger and more abundantly expressed in fetal ECs (Figure S2F). This difference was confirmed in sorted ECs from the labyrinth (fetal) and the decidua (maternal) placental zones (Figure S2G). Moreover, the quantification of DNA methylation revealed increased DNA methylation levels in the labyrinth zone compared with other placental compartments, coinciding with DNMT3A expression (Figures 2E and 2F). Together, these experiments underlined that DNMT3A serves as the main DNMT in labyrinth ECs, whose expression is controlled in a blood flow-dependent manner.

Loss of *Dnmt3a* results in DNA hypomethylation and associated transcriptional deregulation

Considering the trophoblasts' known capacity for vascular mimicry, characterized by their expression of vascular markers such as *Tek*, *Kdr*, *Flt1*, *Eng* and *Vwf* (Figure S2H), we specifically examined the expression pattern activated by the Cre driver used in alternative cell types. Although we observed robust CDH5 expression in labyrinth ECs co-localizing with CD31 (Figure S2I), our analysis also revealed CDH5 expression in EC-adjacent cells (Figure S2J). Notably, through analysis of published single-nuclei RNA-seq data from mouse placental tissue, we identified *Cdh5* expression in trophoblast and decidual cells (Figure S2K). Consequently, due to the observed lack of Cre driver specificity, experiments involving *Cdh5*-Cre crossed to *Dnmt3a*-floxed mice were designated as EC-predominant rather than EC-specific. As *Dnmt3a* was ubiquitously expressed across all placenta cell types (Figure S2L), it is essential to acknowledge the possibility of an impact resulting from the loss of *Dnmt3a* specifically within trophoblast cells. Although our analysis confirms *Dnmt3a*'s widespread expression, transcriptome analysis of *Dnmt3a* knockout extra-embryonic ectoderm at E7.5 revealed in total 10 differentially expressed genes (DEGs) compared with wildtype controls (>1.5 fold change).[19] Therefore, we focused our analysis on *Dnmt3a*'s effect in ECs.

To assess the relevance of DNA methylation introduced via DNMT3A, we profiled fluorescence-activated cell sorting (FACS)-sorted labyrinth ECs isolated from *Dnmt3a*-floxed mice (*Dnmt3a*^{fl/fl}) crossed to *Cdh5*-Cre mice resulting in the loss of *Dnmt3a* predominantly in vascular ECs of *Cdh5*-Cre positive embryos (referred to as Cre[+]) (Figure 3A). The specific dissection of the labyrinth ensured the isolation of fetal-derived ECs (either Cre[+] or Cre[−]) without contamination by maternal ECs (Fig-

ure S3A). As anticipated, loss of *Dnmt3a* in ECs resulted in reduced DNA methylation (average DNA methylation of 74.3% for Cre[−] and 72.2% for Cre[+] ECs) (Figures S3B and S3C). Notably, the main difference was observed based on the sampled genotype and not on the sex of the embryo (Figure S3D). In total, we identified 2,401 hypomethylated differentially methylated regions (DMRs) in *Dnmt3a*-null ECs (Cre[+]) compared with Cre[−] ECs (Figure 3B). Identified DMRs were mainly enriched in intronic regions, as well as in regions 1–5 kb upstream of the transcription start site (TSS), CpG shores, and promoters (Figure 3C). Notably, DMRs often spanned more than one genomic feature. The observed enrichment in potential regulatory elements and promoters itself pointed to potential gene deregulation. Therefore, we performed RNA-seq analysis on labyrinth ECs from the same mouse line and same embryonic age (Figure 3A). This analysis identified 480 DEGs (adj. $p < 0.05$; 303 genes $\log_2FC > 0$ and 177 genes $\log_2FC < 0$), which showed an enrichment for the biological processes of cell motility, circulatory system development, and locomotion (Figures 3D and 3E). Interestingly, among the top upregulated genes in *Dnmt3a*-null ECs we identified *Sema3b* (Figure S3E), known for its inhibitory function in angiogenesis.[40]

To analyze whether DNA hypomethylation was causally involved in the observed gene deregulation, we integrated the methylome and transcriptome data (Figure 3A). This resulted in 105 genes that showed a significant expression change associated with DNA hypomethylation in *Dnmt3a*-null ECs (Figure 3F). Notably, no association was observed for the rare event of DNA hypermethylation (22 DMRs; Figure 3B). To further specify the impact of affected genes in the organization of the placental vasculature, we assessed the expression score of DEGs upon *Dnmt3a* loss in the identified placental EC pseudospace. This revealed an enrichment of DNMT3A-dependent DEGs in ECs of the intermediate-space of the placenta (Figure 3G). Notably, *Lyve1* and *Unc5b*, with an expression peak in the intermediate EC cluster (Figures 1C and 1D), were deregulated upon loss of *Dnmt3a*. Staining of tissue sections confirmed the significant reduction of LYVE1 in ECs (CD31 positive) of the murine placenta labyrinth layer upon *Dnmt3a* deletion in ECs (Figures 3H and 3I). The reduction of LYVE1 in the labyrinth endothelium was also evident upon global deletion of *Dnmt3a* (Figures S3F and S3G). These data suggest that DNMT3A is involved in the establishment of DNA methylation in the labyrinth endothelium of the mature placenta and that loss of DNMT3A-dependent DNA methylation results in deregulation of critical genes in ECs close to the maternal-facing side.

Loss of endothelial *Dnmt3a* impairs developmental growth and reduces angiogenesis

We next examined the vascular phenotype of mice with EC-predominant and global loss of *Dnmt3a* (Figure S3A). The EC-predominant loss of *Dnmt3a* resulted in reduced labyrinth vascular outgrowth (Figure 4A) and reduced embryo weight at E16.5

(H) Representative images of E16.5 *Dnmt3a*^{fl/fl} and *Dnmt3a*^{fl/fl}×*Cdh5*-Cre placentas stained for CD31 and LYVE1. M, maternal; J, junctional; L, labyrinth compartment. Scale bar: 200 μm.
(I) Quantification of LYVE1/CD31 in the labyrinth area of E16.5 placentas from *Dnmt3a*^{fl/fl} and *Dnmt3a*^{fl/fl}×*Cdh5*-Cre embryos. $n \geq 4$. Shown are mean ± SD. The statistical significance was assessed by Mann-Whitney test (I). **$p < 0.01$.
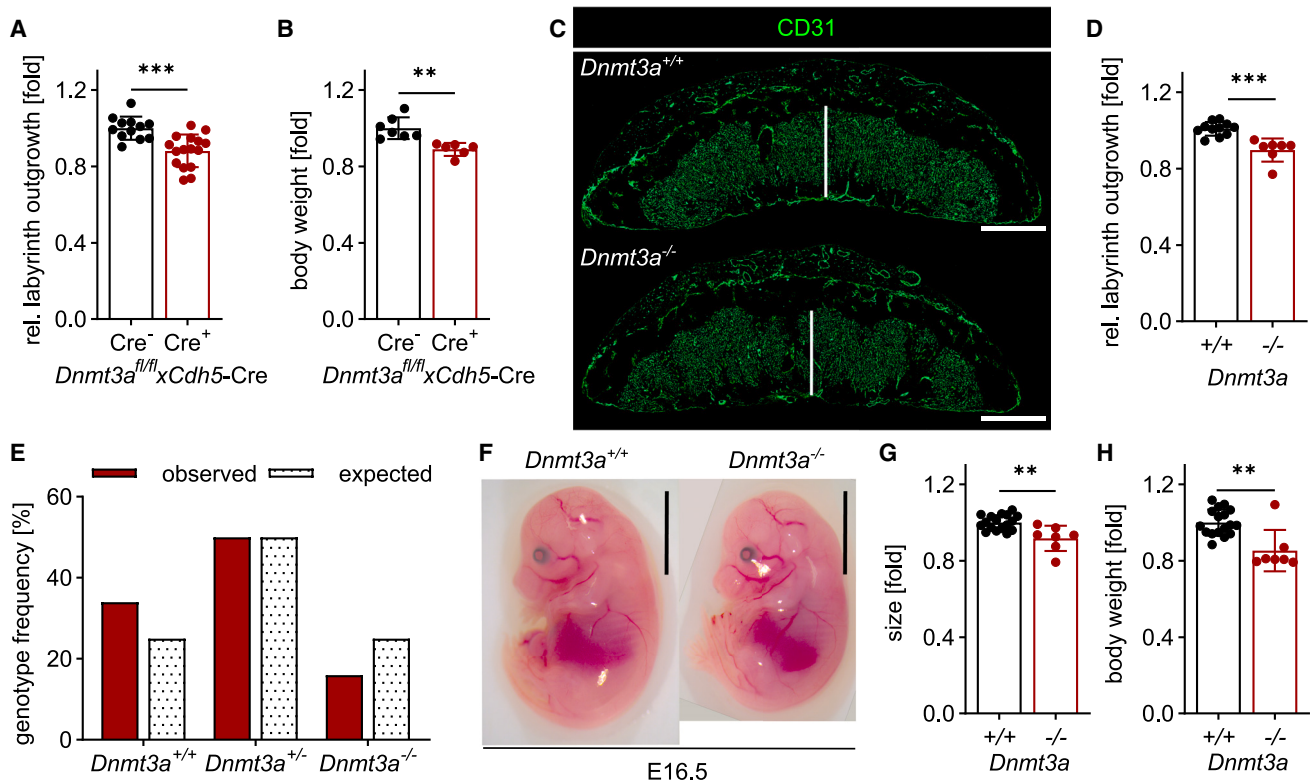
Figure 4. Loss of *Dnmt3a* results in reduced placenta vascularization and growth impairment during late embryonic development
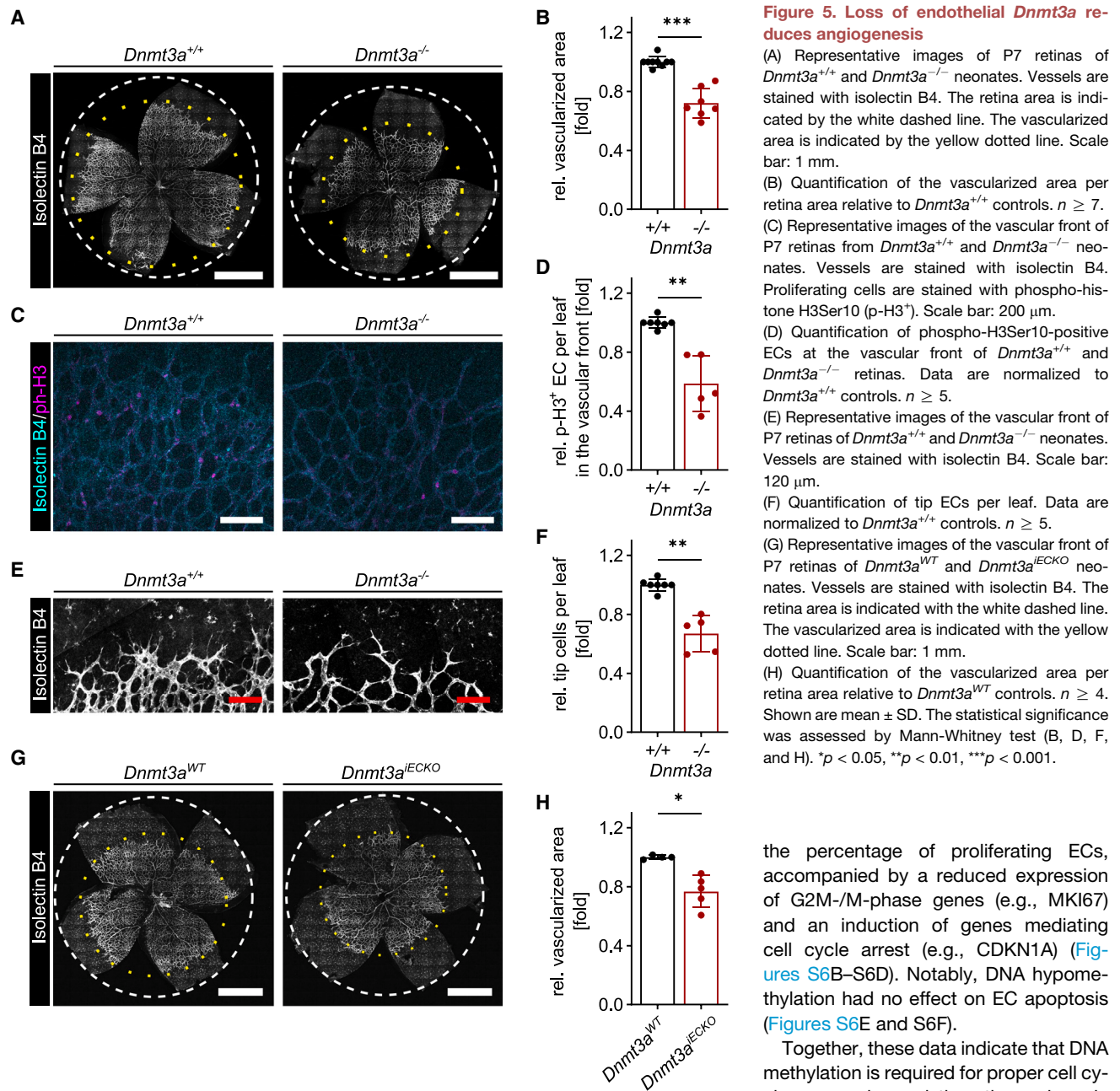
(A) Quantification of labyrinth outgrowth at E16.5 in *Dnmt3a^{fl/fl}* placentas expressing *Cdh5*-Cre (Cre$^+$) or not (Cre$^-$). Data are normalized to *Dnmt3a^{fl/fl}* controls and per litter. $n \geq 6$.

(B) Quantification of embryo weight at E16.5 of *Dnmt3a^{fl/fl}* mice expressing *Cdh5*-Cre (Cre$^+$) or not (Cre$^-$). Data are normalized to *Dnmt3a^{fl/fl}* controls and per litter. $n \geq 6$.

(C) Representative images of E16.5 *Dnmt3a^{+/+}* and *Dnmt3a^{-/-}* placentas stained for the EC marker CD31. Labyrinth outgrowth is indicated with white bars. Scale bar: 1mm.

(D) Quantification of labyrinth outgrowth at E16.5 of *Dnmt3a^{+/+}* and *Dnmt3a^{-/-}* placentas. Data are normalized to *Dnmt3a^{+/+}* controls and per litter. $n \geq 7$.

(E) Genotype frequency at E16.5 of offspring from Dnmt3a$^{+/-}$ mice crossing showing a significant deviation from the expected Mendelian ratio (chi-square test, $\chi^2 = 9.058$, $p = 0.011$). $n = 138$ embryos from 17 pregnant mice.

(F) Representative images of *Dnmt3a^{+/+}* and *Dnmt3a^{-/-}* E16.5 embryos. Scale bar: 0.5 cm.

(G) Quantification of *Dnmt3a^{+/+}* and *Dnmt3a^{-/-}* embryo size at E16.5. Data are normalized to *Dnmt3a^{+/+}* controls and per litter. $n \geq 7$.

(H) Quantification of *Dnmt3a^{+/+}* and *Dnmt3a^{-/-}* embryo body weight at E16.5. Data are normalized to *Dnmt3a^{+/+}* controls and per litter. $n \geq 7$. Shown are mean ± SD. The statistical significance was assessed by Mann-Whitney test (A, B, D, G, and H). **$p < 0.01$, ***$p < 0.001$.

(Figure 4B). *Pecam1* expression (used as a marker of EC identity) in FACS-sorted ECs was unaffected (Figure S4A), indicating the maintenance of EC identity. Other vascular parameters, such as the vascularized area within the labyrinth, the vessel lumen, and the extravascular space,were not changed upon EC-predominant *Dnmt3a* loss (Figures S4B–S4D), suggesting no major vascular defects. Notably, the size of the embryos was unchanged (Figure S4E).

The analysis of the labyrinth compartment of global *Dnmt3a* knockout (KO) placentas (*Dnmt3a^{-/-}*) at E16.5 (Figure S3A) confirmed the reduced vascular outgrowth in *Dnmt3a^{-/-}* compared with *Dnmt3a^{+/+}* control placentas (Figures 4C and 4D). The vascular loss was also reflected in declined *Cd31* expression levels in total placenta tissue of *Dnmt3a^{-/-}* embryos (Figure S4F), which was not attributed to increased apoptosis in *Dnmt3a^{-/-}* placentas (Figures S4G and S4H). Mating of mice heterozygous for the *Dnmt3a*-null allele resulted in 16% *Dnmt3a* KO embryos at E16.5, representing a significant deviation from the expected Mendelian ratio, which was not detectable at E10.5 (Figures 4E and S4I). As the fetus switches from yolk sac to placental nutrition from day E10 onward, this late *Dnmt3a* KO phenotype suggested a specific defect in placental function.[3] Similar to the EC-predominant *Dnmt3a* loss, the size and weight of *Dnmt3a* KO embryos were significantly reduced at E16.5 (8.2% average reduction in size; 14.7% average reduction in weight), but not at E10.5 compared with *Dnmt3a^{+/+}* control littermates, indicating a growth delay (Figures 4F–4H, S4J, and S4K).

To study the angiogenic potential of the *Dnmt3a*-deficient endothelium, we analyzed the vascularization of the retina in neonatal mice.[41] Upon loss of *Dnmt3a*, the vascularized area of the retina was significantly reduced in *Dnmt3a^{-/-}* compared with *Dnmt3a^{+/+}* control retinas (Figures 5A, 5B, and S5A). More detailed characterization revealed a reduction in proliferating ECs and tip cells at the front of invading capillaries (Figures 5C–5F and S5B). The same phenotype was observed

Figure 5. Loss of endothelial *Dnmt3a* reduces angiogenesis

(A) Representative images of P7 retinas of *Dnmt3a*$^{+/+}$ and *Dnmt3a*$^{-/-}$ neonates. Vessels are stained with isolectin B4. The retina area is indicated by the white dashed line. The vascularized area is indicated by the yellow dotted line. Scale bar: 1 mm.

(B) Quantification of the vascularized area per retina area relative to *Dnmt3a*$^{+/+}$ controls. $n \geq 7$.

(C) Representative images of the vascular front of P7 retinas from *Dnmt3a*$^{+/+}$ and *Dnmt3a*$^{-/-}$ neonates. Vessels are stained with isolectin B4. Proliferating cells are stained with phospho-histone H3Ser10 (p-H3$^+$). Scale bar: 200 μm.

(D) Quantification of phospho-H3Ser10-positive ECs at the vascular front of *Dnmt3a*$^{+/+}$ and *Dnmt3a*$^{-/-}$ retinas. Data are normalized to *Dnmt3a*$^{+/+}$ controls. $n \geq 5$.

(E) Representative images of the vascular front of P7 retinas of *Dnmt3a*$^{+/+}$ and *Dnmt3a*$^{-/-}$ neonates. Vessels are stained with isolectin B4. Scale bar: 120 μm.

(F) Quantification of tip ECs per leaf. Data are normalized to *Dnmt3a*$^{+/+}$ controls. $n \geq 5$.

(G) Representative images of the vascular front of P7 retinas of *Dnmt3a*^{WT} and *Dnmt3a*^{iECKO} neonates. Vessels are stained with isolectin B4. The retina area is indicated with the white dashed line. The vascularized area is indicated with the yellow dotted line. Scale bar: 1 mm.

(H) Quantification of the vascularized area per retina area relative to *Dnmt3a*^{WT} controls. $n \geq 4$. Shown are mean ± SD. The statistical significance was assessed by Mann-Whitney test (B, D, F, and H). *$p < 0.05$, **$p < 0.01$, ***$p < 0.001$.

the percentage of proliferating ECs, accompanied by a reduced expression of G2M-/M-phase genes (e.g., MKI67) and an induction of genes mediating cell cycle arrest (e.g., CDKN1A) (Figures S6B–S6D). Notably, DNA hypomethylation had no effect on EC apoptosis (Figures S6E and S6F).

Together, these data indicate that DNA methylation is required for proper cell cycle progression and, thus, the angiogenic capacity of ECs. Moreover, *Dnmt3a* serves as a critical epigenetic regulator of placental labyrinth and retinal vascularization.

Dnmt3a loss is associated with placental dysfunction in mice

According to the original report, global embryonic *Dnmt3a* deficiency leads to a reduced size of neonatal mice, eventually causing an early postnatal death at about 1 month of age.[18] We also observed a sub-Mendelian percentage of newborn homozygous *Dnmt3a*-null mice as well as reduced size and weight of *Dnmt3a*-deficient neonates compared with their wildtype littermates (Figures S7A–S7D). Yet, although the global *Dnmt3a*-deficient pups were smaller and lighter compared with their wildtype
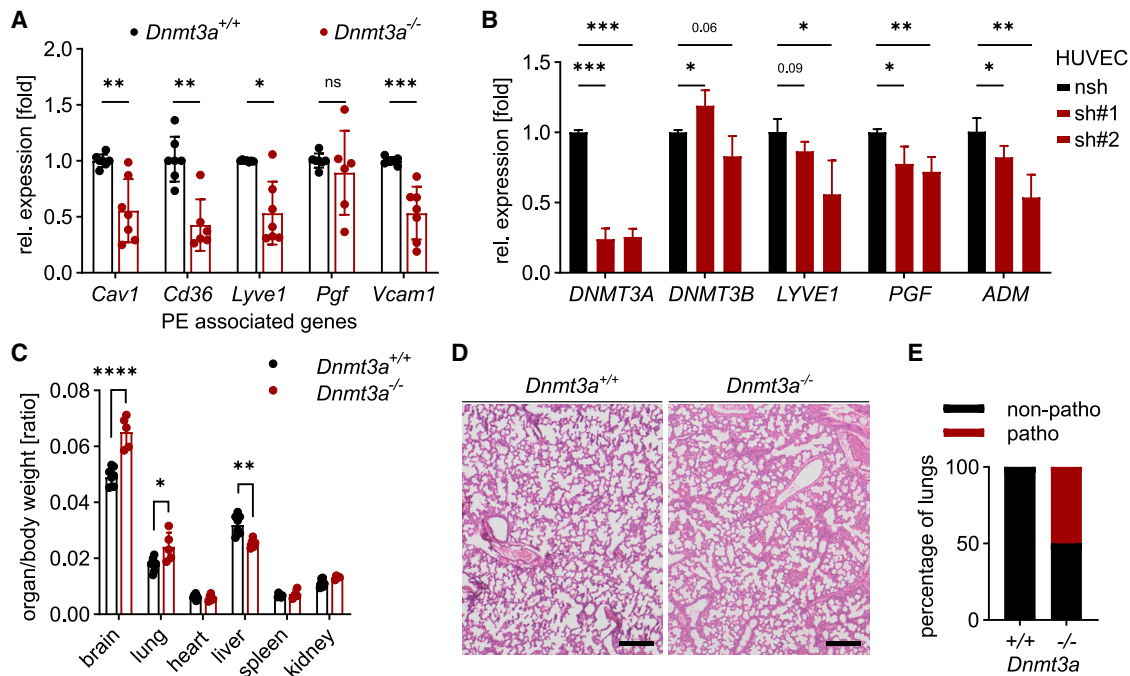
in a mouse model with EC-specific postnatal deletion of *Dnmt3a* via administration of hydroxytamoxifen to newborn *Dnmt3a*$^{fl/fl}$ × *Cdh5*-Cre^{ERT2} mice (*Dnmt3a*^{iECKO}) (Figures 5G, 5H, and S5C–S5G). This surrogate model of postnatal developmental angiogenesis unambiguously confirmed endothelial *Dnmt3a* as a critical regulator of angiogenesis.

To gain mechanistic insight into direct effects of DNA hypomethylation on EC function, DNA hypomethylation was induced by consecutive treatment of HUVECs with the DNMT inhibitor, decitabine (DEC). Of note, the *de novo* DNMTs, DNMT3A and DNMT3B, were found to show a higher sensitivity to DEC compared with DNMT1 in mouse embryonic stem cells.[42] The loss of DNA methylation (Figure S6A) significantly decreased

Developmental Cell
Article

Figure 6. Loss of *Dnmt3a* is associated with a preeclampsia-like phenotype in mice

(A) Relative expression of genes associated with preeclampsia in murine E16.5 total placenta tissue from *Dnmt3a*^{+/+} and *Dnmt3a*^{−/−} mice. $n = 7$.

(B) Relative expression of genes associated with preeclampsia in HUVECs upon lentiviral transduction with *shDNMT3A* (sh#1, sh#2) or control shRNA (nsh) constructs, respectively. $n = 3$.

(C) Organ-to-body weight ratio measured in *Dnmt3a*^{+/+} and *Dnmt3a*^{−/−} mice at P9. $n \geq 5$.

(D) Representative H&E stainings of lung tissue at P9 from *Dnmt3a*^{+/+} and *Dnmt3a*^{−/−} mice. Scale bar: 200 μm.

(E) Analysis of lung tissue at P9 by a board-certified pathologist (C.M.). "Non-patho" = no pathological changes, "patho" = immune infiltrates and/or fibrosis in *Dnmt3a*^{+/+} and *Dnmt3a*^{−/−} mice. $n \geq 4$. Data are shown as mean ± SD. The statistical significance was assessed by Mann-Whitney test (A, and C) or unpaired t test (B). *$p < 0.05$, **$p < 0.01$, ***$p < 0.001$, ****$p < 0.0001$.

littermates, EC-specific *Dnmt3a*^{fl/fl}×*Cdh5*-Cre neonates were similar in size compared with their *Dnmt3a*^{fl/fl} littermates and only showed a mildly reduced body weight (Figures S7E and S7F).

To assess placental function upon deletion of *Dnmt3a*, we zoomed in on genes that have been reported to be dysregulated in human placental dysfunction.[43–47] Many of the reported genes related to placenta dysfunction are well-known vascular genes, such as *Cav1* and *Cd36*, which are mainly expressed in the endothelium of the placenta (Figures S7G and S7H). Indeed, *Cav1*, *Cd36*, *Lyve1*, *Pgf*, and *Vcam1* were downregulated in E16.5 placenta tissue of *Dnmt3a*^{−/−} compared with *Dnmt3a*^{+/+} control placentas (Figure 6A).

To elucidate whether the expression of these genes is dependent on the presence of *Dnmt3a* in ECs, *DNMT3A* expression was silenced via two independent short hairpin RNAs (shRNAs) in cultured HUVECs. Gene expression analysis demonstrated a significant downregulation of several genes associated with placenta insufficiency in ECs but not in trophoblasts silenced for *DNMT3A* expression (Figures 6B, S7I, and S7J). Further organ analysis of *Dnmt3a*^{−/−} compared with *Dnmt3a*^{+/+} control neonates revealed a significantly heavier brain which indicates brain sparing—a well-known indication of nutrient deprivation as a consequence of placenta insufficiency (Figure 6C).[48] Additionally, 50% of the lungs resected from *Dnmt3a*^{−/−} pups showed signs of immune infiltrates and fibrosis (Figures 6D

and 6E). In summary, these expression and postnatal analyses suggest that the loss of *Dnmt3a* contributes to vascular and, thus, placental dysfunction.

Reduced *DNMT3A* expression in human placenta ECs is associated with PE

To corroborate whether the results of the analytical and manipulatory mouse experiments have implications for the mechanistic understanding of endothelial function in the human placenta during health and disease, we performed a re-analysis of public single-cell RNA-seq data of 1,368 and 756 ECs sampled from full-term and early preeclamptic human placentas, respectively.[49] Congruent marker expression in the healthy placenta enabled the identification of cell populations, including different types of trophoblasts lineages and ECs (Figure 7A). To assess the importance of distinct epigenetic mechanisms in different placenta cell types, the expression of genes involved in writing, reading, or erasing epigenetic marks (chromatin remodeling, histone modification, and DNA modification[50]) was analyzed (Table S1). The expression of DNA methylation modifiers such as *DNMT1*, *GADD45B*, and *MGMT* was highest in Hofbauer cells, ECs, and trophoblasts, indicating an important role of DNA methylation modification in those cell types (Figure S8A and S8B). Of the *de novo* DNMTs, *DNMT3A*, but not *DNMT3B* was highly expressed in placenta
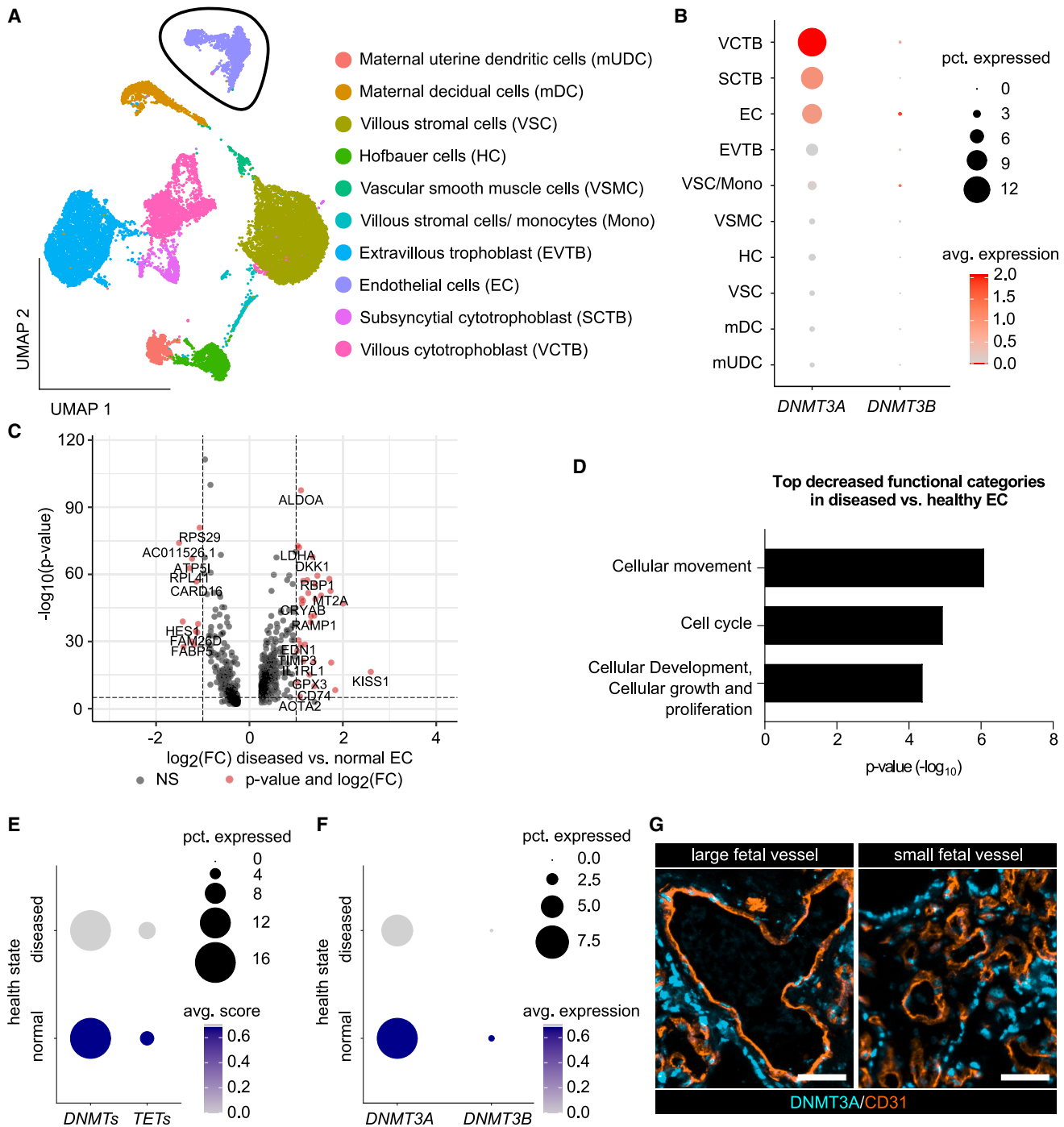
Figure 7. Reduced *DNMT3A* expression in human placenta ECs is associated with preeclampsia

(A) UMAP of healthy human placenta single-cell data[49] with cell type annotation based on marker gene expression. Endothelial cells are encircled in black.

(B) Expression of *DNMT3A* and *DNMT3B* in different cell types of healthy human placenta. Cell types are sorted in descending order according to the percentage of cells expressing *DNMT3A*.

(C) Volcano plot visualizing the gene expression changes (717 genes total) between diseased (= preeclampsia) and healthy placenta ECs (red dots indicate significantly differentially expressed genes). The cutoff for the p value ($10e^{-6}$) is indicated by a dashed horizontal line; the fold change (FC) cutoff (2) is indicated by dashed vertical lines.

(D) Top decreased functional categories attributed to the genes differentially expressed in diseased vs. healthy placenta ECs (ingenuity pathway analysis, QIAGEN). Adj. p value < 0.05.

(legend continued on next page)

Developmental Cell
Article

🔓 **CellPress**
OPEN ACCESS

cells, particularly in trophoblasts and ECs (Figure 7B). These data imply DNMT3A as a key epigenetic DNA methylation modifier in the human placental endothelium.

To gain insight into the role of ECs in human placenta dysfunction, differential transcriptome analysis of healthy vs. diseased ECs from preeclamptic placentas was performed. This revealed 356 upregulated and 192 downregulated genes in preeclamptic vs. healthy ECs (Figure 7C). The functional annotation of these DEGs showed a significant decrease in the pro-angiogenic endothelial functions "cellular movement" and "cell cycle" (Figure 7D). Further analysis focused on DNA methylation regulators and revealed a reduction of ECs expressing DNA methylation writers (*DNMT3A* and *DNMT3B*) in preeclamptic placentas, especially of *DNMT3A* (Figures 7E and 7F). In the healthy human placenta, DNMT3A was abundantly expressed in the endothelium of both, large and small vessels in the fetal compartment (Figure 7G). Fetal capillaries can be found in the chorionic villi of the human placenta. As this network of fetal capillaries is essential for gas and nutrient exchange between maternal and fetal blood, the presented data suggest a role of endothelial DNMT3A in the regulation of mature placenta function. Consequently, the reduced *DNMT3A* expression in PE ECs might contribute to placenta insufficiency with compromised fetal growth.

DISCUSSION

This study identified the so far unknown flow-dependent spatial gene expression pattern in the murine placental vasculature of the fetal-derived labyrinth compartment. The data show that DNA methylation is involved in the nuanced transcriptional changes upon blood flow conditions. We discovered that DNMT3A acts as the main *de novo* DNMT in the vasculature and directs proper spatially zonated placental gene expression. Blood flow-controlled hemodynamic forces and luminal pressure are sensed and translated into functional and morphological changes via mechanotransduction.[51] The flow-mediated epigenetic modulation of the endothelium was first reported during embryonic heart development[52] and in different cardiovascular diseases.[51,53] Interestingly, DNA methylation changes in mice, which are prone to develop atherosclerosis, have been detected prior to the onset of disease.[54] Mechanistically, disturbed blood flow results in suppression of the atheroprotective transcription factor KLF4 via DNMT3A-mediated promoter hypermethylation.[36] Therefore, modifiers of the epigenetic landscape, especially DNA methylation, might have the potential to function as biomarkers of vascular pathologies, which are associated with disturbed blood flow.

Placenta insufficiency may lead to FGR or PE. The importance of adequate epigenetic regulation of placenta development, particularly in terms of the resulting DNA methylation profile, has recently received considerable attention.[15,55,56] This study took advantage of published single-cell RNA-seq data of human,[49] and single-nuclei RNA-seq data of mouse[39] placenta.

Our vascular-centered analysis suggests that placental dysfunction is associated with reduced expression of DNMT3A in the fetal endothelium of mice and humans.

Proper DNA methylation is essential in placenta and fetal development. Upon fertilization, initial global demethylation is followed by *de novo* DNA methylation, predominantly in cells with fetal fate, resulting in global hypermethylation of fetal cells compared with other placental cells.[13,57–59] Based on these findings, fetal cells in the placenta are likely the most susceptible cell population to widespread loss of *de novo* DNA methylation. Along the same line, we showed that the fetoplacental endothelium expressed high levels of *DNMT3A* in healthy placentas. Likewise, the loss of DNMT3A-dependent DNA methylation in the endothelium resulted in decreased labyrinth vascularization and fetal growth defects. Thus, several lines of evidence suggest that *de novo* DNA methylation in the fetal endothelium plays a crucial role in placental maturation and may thereby contribute to proper fetal nourishment. Based on this notion, our data imply that a dysfunctional fetoplacental vasculature is central in placental dysfunction, reflecting the consequences of a disturbed maternal-fetal interface.

The causal involvement of the fetoplacental vasculature in the pathogenesis of placental dysfunction has stimulated research aimed at exploiting dysregulated endothelial-specific genes as potential predictive markers for the early identification of pregnant women at risk of developing PE.[60] Elevated levels of soluble intercellular adhesion molecule 1 (ICAM1) and vascular cell adhesion molecule 1 (VCAM1) have been reported in pregnant women 8–12 weeks prior to developing clinical symptoms of PE,[61] establishing sICAM1 and sVCAM1 as some of the most sensitive and specific predictive markers of PE.[62] Likewise, aberrant levels of circulating placental growth factor (PGF) and soluble fms-like tyrosine kinase 1 (sFlt1) have been proposed as prognostic markers of PE.[63,64] These biomarkers studies support the vascular pathogenesis of the most critical pregnancy-related diseases. This study adds to these concepts by contributing important insight into the molecular mechanisms of placental vascular adaptation and remodeling during pregnancy.

Several studies have reported that aberrant DNA methylation is associated with placenta-related pathologies.[8–10] Recent studies have associated reduced levels of DNMT3A with placental insufficiency.[24,25] Specific hypomethylation patterns were observed in placentas of pregnancies diagnosed with IUGR[11] and in cell-free DNA (cfDNA) in plasma samples collected from patients with PE for predicted fetal placental genomic regions.[65] Notably, cfDNA hypomethylation in PE near genes such as *NFATC2*, *HOXA7*, and *NAV2* were also observed in murine ECs lacking *Dnmt3a* expression. Furthermore, a predominant DNA hypomethylation in placentas obtained from women diagnosed with PE was especially close to genes associated with cardiovascular-metabolic developmental pathways.[66] The link between DNA hypomethylation and placental vascular dysfunction was underlined by cfDNA methylation changes

(E) Scored expression of DNA methylation writers (DNMTs) and editors (TETs) in ECs of normal and diseased placentas. Pct. expression refers to the percentage of cells in a cluster expressing the assigned score and avg. expression refers to the average expression level.

(F) Expression of *de novo* DNA methyltransferases in ECs of normal and diseased placentas. Pct. expression refers to the percentage of cells in a cluster expressing the shown gene and avg. expression refers to the average expression level.

(G) Co-staining of CD31 and DNMT3A on healthy human placenta tissue (chorionic villus zone). Scale bar: 50 μm.

near genes associated with placental blood vessel formation in PE.[65] Interestingly, DNA hypomethylation was found in regulatory elements in patients with PE,[67–69] indicating the importance of DNA methylation in regulating gene expression for normal development. However, the general lack of genome-wide DNA methylation studies that include sample-matched transcriptome data does not allow a functional association between the reduction of DNMT3A and DNA methylation alterations.

In summary, this study identified that the murine placental vasculature shows a gradual change in gene expression which matches their spatial localization from the fetal- toward the maternal-facing labyrinth side. Furthermore, we discovered that endothelial DNMT3A represents an epigenetic regulator in the placenta vasculature that affects the spatial gene expression pattern. By establishing an appropriate DNA methylation landscape, DNMT3A is required to maintain the angiogenic capacity of ECs and appropriate tissue vascularization. Finally, loss of *Dnmt3a* in the endothelium can be associated with placenta dysfunction resulting in reduced fetal growth in mice. Thus, our study provides mechanistic insight into the role of the fetoplacental vasculature in general, and *Dnmt3a*, especially in controlling placenta vascularization.

Limitations of the study

Certain limitations need to be acknowledged. First, the lack of organ- and cell-specific loss-of-function mouse models prevented a direct test of whether the observed growth retardation resulted exclusively from a decrease in the labyrinth vasculature. Consequently, we cannot exclude a delay in angiogenesis in the embryos themselves with global or endothelial-predominant deletion of *Dnmt3a*. To specifically target placental ECs without affecting ECs and their precursors derived from the embryo, the *Hoxa13*-Cre[70] model crossed with *Dnmt3a*-floxed mice could be used. This approach would allow for a focused investigation of the developmental effects resulting from the loss of *Dnmt3a* in the placental endothelium, thereby addressing the limitations associated with broader EC targeting in the study. Additionally, the study focused on the effects of *Dnmt3a* loss in ECs and did not analyze other cell types like trophoblasts, which are known for vascular mimicry and express important vascular genes.[71] Due to the known leakiness of the used *Cdh5*-Cre mouse line into the trophoblast lineage, we cannot entirely rule out the possibility of defects in trophoblasts upon *Dnmt3a* deletion. However, examination of the extra-embryonic ectoderm in *Dnmt3a* KO embryos, which includes trophoblasts, showed only minor effects on the methylome and transcriptome compared with wildtype controls.[19] However, the observed ubiquitous expression of *Dnmt3a* underlines the need for further exploration to fully assess the potential consequences of *Dnmt3a* deficiency in trophoblasts. The study also did not consider potential confounding variables such as the sex of the embryos and pups in the mouse experiments. In human pregnancies, fetal gender influences sex-specific variations in fetal parameters like biparietal diameter, head circumference, abdominal circumference, and fetal weight, with male fetuses typically larger than females from early gestational stages.[72,73] It remains uncertain whether observed sex-specific growth differences result from fetal sex determining placental function or whether sexual dimorphism in placental function influences fetal growth. Additionally, the relationship

between fetal sex and pregnancy complications like PE remains unclear, with conflicting findings in the literature.[74–77] Overall, although the study provides valuable insights, addressing these limitations will be crucial for a more comprehensive understanding of placental biology and associated diseases.

RESOURCE AVAILABILITY

Lead contact
Requests for further information and resources should be directed to and will be fulfilled by the lead contact, Hellmut G. Augustin (augustin@angioscience.de).

Materials availability
This study did not generate new unique reagents.

Data and code availability
Single-cell raw data and count matrices generated in this study are publicly available under the GEO accession number: GSE280168. Bulk RNA-seq raw data, annotated reads, and the DESeq2 results are accessible under GEO accession number: GSE280085. WGBS raw data, unfiltered ß-values, and called DMRs are publicly available under the following GEO accession number: GSE280086. This study does not report original code. Any additional information required to reanalyze the data reported in this work paper is available from the lead contact upon request.

AUTHOR CONTRIBUTIONS

S.G., H.G.A., and K.S. conceived the study. S.G., E.G., D.W., and C.M. performed the experiments. S.G., M.J., Z.G., and K.S. analyzed sequencing data. S.G. wrote the original draft of the manuscript. M.J., E.G., Z.G., D.W., C.M., M.S., C.P., K.S., and H.G.A. reviewed and edited the manuscript. K.S. and H.G.A supervised the study and acquired the funding.

DECLARATION OF INTERESTS

The other authors declare no competing interests.

STAR★METHODS

Detailed methods are provided in the online version of this paper and include the following:

- KEY RESOURCES TABLE
- EXPERIMENTAL MODEL AND STUDY PARTICIPANT DETAILS

Developmental Cell
Article

CellPress
OPEN ACCESS

- ○ Mice
- ○ Human sample collection
- ● METHOD DETAILS
  - ○ EC isolation by FACS
  - ○ Whole genome bisulfite sequencing (WGBS)
  - ○ Singel-cell library generation and sequencing
  - ○ RNA-sequencing
  - ○ RNA isolation, reverse transcription, and quantitative measurement
  - ○ Retina angiogenesis assay
  - ○ Histology
  - ○ Cell culture and *in vitro* studies
  - ○ DNA methylation analysis via dot blot
- ● QUANTIFICATION AND STATISTICAL ANALYSIS
  - ○ Quantification of vessel parameters in the murine placenta
  - ○ Quantitative PCR analysis
  - ○ Quantification of global DNA methylation changes assessed via dot blot
  - ○ Human single-cell data analysis
  - ○ Murine placenta single-cell data analysis
  - ○ Murine labyrinth EC single-cell data analysis
  - ○ RNA-seq analysis
  - ○ WSBS analysis
  - ○ Statistical analysis

SUPPLEMENTAL INFORMATION

Supplemental information can be found online at https://doi.org/10.1016/j.devcel.2024.12.037.

REFERENCES

1. Rossant, J., and Cross, J.C. (2001). Placental development: Lessons from mouse mutants. Nat. Rev. Genet. 2, 538–548. https://doi.org/10.1038/35080570.

2. Georgiades, P., Ferguson-Smith, A.C., and Burton, G.J. (2002). Comparative developmental anatomy of the murine and human definitive placentae. Placenta 23, 3–19. https://doi.org/10.1053/PLAC.2001.0738.

3. Woods, L., Perez-Garcia, V., and Hemberger, M. (2018). Regulation of placental development and its impact on fetal growth—new insights from mouse models. Front. Endocrinol. (Lausanne) 9, 570. https://doi.org/10.3389/fendo.2018.00570.

4. Roberts, D.J., and Post, M.D. (2008). The placenta in pre-eclampsia and intrauterine growth restriction. J. Clin. Pathol. 61, 1254–1260. https://doi.org/10.1136/JCP.2008.055236.

5. Huppertz, B., and Peeters, L.L.H. (2005). Vascular biology in implantation and placentation. Angiogenesis 8, 157–167. https://doi.org/10.1007/s10456-005-9007-8.

6. Kingdom, J., Huppertz, B., Seaward, G., and Kaufmann, P. (2000). Development of the placental villous tree and its consequences for fetal growth. Eur. J. Obstet. Gynecol. Reprod. Biol. 92, 35–43. https://doi.org/10.1016/S0301-2115(00)00423-1.

7. Rana, S., Lemoine, E., Granger, J.P., and Karumanchi, S.A. (2019). Preeclampsia: pathophysiology, challenges, and perspectives. Circ. Res. 124, 1094–1112. https://doi.org/10.1161/CIRCRESAHA.118.313276.

8. Nelissen, E.C.M., van Montfoort, A.P.A., Dumoulin, J.C.M., and Evers, J.L.H. (2011). Epigenetics and the placenta. Hum. Reprod. Update 17, 397–417. https://doi.org/10.1093/HUMUPD/DMQ052.

9. Cirkovic, A., Garovic, V., Milin Lazovic, J., Milicevic, O., Savic, M., Rajovic, N., Aleksic, N., Weissgerber, T., Stefanovic, A., Stanisavljevic, D., and Milic, N. (2020). Systematic review supports the role of DNA methylation in the pathophysiology of preeclampsia: A call for analytical and methodological standardization. Biol. Sex Differ. 11, 36. https://doi.org/10.1186/s13293-020-00313-8.

10. Wilson, S.L., Leavey, K., Cox, B.J., and Robinson, W.P. (2018). Mining DNA methylation alterations towards a classification of placental pathologies. Hum. Mol. Genet. 27, 135–146. https://doi.org/10.1093/HMG/DDX391.

11. Banister, C.E., Koestler, D.C., Maccani, M.A., Padbury, J.F., Houseman, E.A., and Marsit, C.J. (2011). Infant growth restriction is associated with distinct patterns of DNA methylation in human placentas. Epigenetics 6, 920–927. https://doi.org/10.4161/epi.6.7.16079.

12. Bird, A. (2002). DNA methylation patterns and epigenetic memory. Genes Dev. 16, 6–21. https://doi.org/10.1101/GAD.947102.

13. Santos, F., Hendrich, B., Reik, W., and Dean, W. (2002). Dynamic reprogramming of DNA methylation in the early mouse embryo. Dev. Biol. 241, 172–182. https://doi.org/10.1006/dbio.2001.0501.

14. Santos, F., Hyslop, L., Stojkovic, P., Leary, C., Murdoch, A., Reik, W., Stojkovic, M., Herbert, M., and Dean, W. (2010). Evaluation of epigenetic marks in human embryos derived from IVF and ICSI. Hum. Reprod. 25, 2387–2395. https://doi.org/10.1093/HUMREP/DEQ151.

15. Ehrlich, M., Gama-Sosa, M.A., Huang, L.H., Midgett, R.M., Kuo, K.C., Mccune, R.A., and Gehrke, C. (1982). Amount and distribution of 5-methylcytosine in human DNA from different types of tissues of cells. Nucleic Acids Res. 10, 2709–2721. https://doi.org/10.1093/NAR/10.8.2709.

16. Novakovic, B., Wong, N.C., Sibson, M., Ng, H.K., Morley, R., Manuelpillai, U., Down, T., Rakyan, V.K., Beck, S., Hiendleder, S., et al. (2010). DNA methylation-mediated down-regulation of DNA methyltransferase-1 (DNMT1) is coincident with, but not essential for, global hypomethylation in human placenta. J. Biol. Chem. 285, 9583–9593. https://doi.org/10.1074/jbc.M109.064956.

17. Robinson, W.P., and Price, E.M. (2015). The human placental methylome. Cold Spring Harb. Perspect. Med. 5, a023044. https://doi.org/10.1101/CSHPERSPECT.A023044.

18. Okano, M., Bell, D.W., Haber, D.A., and Li, E. (1999). DNA methyltransferases Dnmt3a and Dnmt3b are essential for de novo methylation and mammalian development. Cell 99, 247–257. https://doi.org/10.1016/S0092-8674(00)81656-6.

19. Andrews, S., Krueger, C., Mellado-Lopez, M., Hemberger, M., Dean, W., Perez-Garcia, V., and Hanna, C.W. (2023). Mechanisms and function of de novo DNA methylation in placental development reveals an essential role for DNMT3B. Nat. Commun. 14, 371. https://doi.org/10.1038/s41467-023-36019-9.

20. Larsen, F., Gundersen, G., Lopez, R., and Prydz, H. (1992). CpG islands as gene markers in the human genome. Genomics 13, 1095–1107. https://doi.org/10.1016/0888-7543(92)90024-M.

21. Deaton, A.M., and Bird, A. (2011). CpG islands and the regulation of transcription. Genes Dev. 25, 1010–1022. https://doi.org/10.1101/GAD.2037511.

22. Greenberg, M.V.C., and Bourc'his, D. (2019). The diverse roles of DNA methylation in mammalian development and disease. Nat. Rev. Mol. Cell Biol. 20, 590–607. https://doi.org/10.1038/s41580-019-0159-6.

23. Dwi Putra, S.E., Reichetzeder, C., Hasan, A.A., Slowinski, T., Chu, C., Krämer, B.K., Kleuser, B., and Hocher, B. (2020). Being born large for gestational age is associated with increased global placental DNA methylation. Sci. Rep. 10, 927. https://doi.org/10.1038/s41598-020-57725-0.

24. Jia, Y., Li, T., Huang, X., Xu, X., Zhou, X., Jia, L., Zhu, J., Xie, D., Wang, K., Zhou, Q., et al. (2017). Dysregulated DNA Methyltransferase 3A upregulates IGFBP5 to suppress trophoblast cell migration and invasion in preeclampsia. Hypertension 69, 356–366. https://doi.org/10.1161/HYPERTENSIONAHA.116.08483.

25. Gu, H., Gao, J., Guo, W., Zhou, Y., and Kong, Q. (2017). The expression of DNA methyltransferases3A is specifically downregulated in chorionic villi of early embryo growth arrest cases. Mol. Med. Rep. 16, 591–596. https://doi.org/10.3892/MMR.2017.6650.

26. Jakab, M., and Augustin, H.G. (2020). Understanding angiodiversity: insights from single cell biology. Development *147*, dev146621. https://doi.org/10.1242/dev.146621.

27. Aizarani, N., Saviano, A., Sagar, Mailly, L., Durand, S., Herman, J.S., Pessaux, P., Baumert, T.F., and Grün, D. (2019). A human liver cell atlas reveals heterogeneity and epithelial progenitors. Nature *572*, 199. https://doi.org/10.1038/S41586-019-1373-2.

28. Boyé, K., Geraldo, L.H., Furtado, J., Pibouin-Fragner, L., Poulet, M., Kim, D., Nelson, B., Xu, Y., Jacob, L., Maissa, N., et al. (2022). Endothelial Unc5B controls blood-brain barrier integrity. Nat. Commun. *13*, 1169. https://doi.org/10.1038/s41467-022-28785-9.

29. Das, R.N., Tevet, Y., Safriel, S., Han, Y., Moshe, N., Lambiase, G., Bassi, I., Nicenboim, J., Brückner, M., Hirsch, D., et al. (2022). Generation of specialized blood vessels via lymphatic transdifferentiation. Nature *606*, 570–575. https://doi.org/10.1038/s41586-022-04766-2.

30. Ruter, D.L., Liu, Z., Ngo, K.M., X, S., Marvin, A., Buglak, D.B., Kidder, E.J., and Bautch, V.L. (2021). SMAD6 transduces endothelial cell flow responses required for blood vessel homeostasis. Angiogenesis *24*, 387–398. https://doi.org/10.1007/S10456-021-09777-7.

31. Watson, O., Novodvorsky, P., Gray, C., Rothman, A.M.K., Lawrie, A., Crossman, D.C., Haase, A., McMahon, K., Gering, M., Van Eeden, F.J.M., et al. (2013). Blood flow suppresses vascular Notch signalling via dll4 and is required for angiogenesis in response to hypoxic signalling. Cardiovasc. Res. *100*, 252–261. https://doi.org/10.1093/CVR/CVT170.

32. Busch, R., Strohbach, A., Pennewitz, M., Lorenz, F., Bahls, M., Busch, M.C., and Felix, S.B. (2015). Regulation of the endothelial apelin/APJ system by hemodynamic fluid flow. Cell. Signal. *27*, 1286–1296. https://doi.org/10.1016/J.CELLSIG.2015.03.011.

33. Maselli, D., Garoffolo, G., Cassanmagnago, G.A., Vono, R., Ruiter, M.S., Thomas, A.C., Madeddu, P., Pesce, M., and Spinetti, G. (2022). Mechanical strain induces transcriptomic reprogramming of saphenous vein progenitors. Front. Cardiovasc. Med. *9*, 884031. https://doi.org/10.3389/fcvm.2022.884031.

34. Zheng, Q., Zou, Y., Teng, P., Chen, Z., Wu, Y., Dai, X., Li, X., Hu, Z., Wu, S., Xu, Y., et al. (2022). Mechanosensitive channel PIEZO1 senses shear force to induce KLF2/4 expression via CaMKII/MEKK3/ERK5 axis in endothelial cells. Cells *11*, 2191. https://doi.org/10.3390/CELLS11142191/S1.

35. Shen, L., Zhou, K., Liu, H., Yang, J., Huang, S., Yu, F., and Huang, D. (2022). Prediction of mechanosensitive genes in vascular endothelial cells under high wall shear stress. Front. Genet. *12*, 796812. https://doi.org/10.3389/FGENE.2021.796812/BIBTEX.

36. Jiang, Y.Z., Jiménez, J.M., Ou, K., McCormick, M.E., Zhang, L.D., and Davies, P.F. (2014). Hemodynamic disturbed flow induces differential DNA methylation of endothelial Kruppel-like factor 4 promoter in vitro and in vivo. Circ. Res. *115*, 32–43. https://doi.org/10.1161/CIRCRESAHA.115.303883/-/DC1.

37. Tsaryk, R., Yucel, N., Leonard, E.V., Diaz, N., Bondareva, O., Odenthal-Schnittler, M., Arany, Z., Vaquerizas, J.M., Schnittler, H., and Siekmann, A.F. (2022). Shear stress switches the association of endothelial enhancers from ETV/ETS to KLF transcription factor binding sites. Sci. Rep. *12*, 4795. https://doi.org/10.1038/s41598-022-08645-8.

38. Jones, P.A. (2012). Functions of DNA methylation: islands, start sites, gene bodies and beyond. Nat. Rev. Genet. *13*, 484–492. https://doi.org/10.1038/nrg3230.

39. Marsh, B., and Blelloch, R. (2020). Single nuclei RNA-seq of mouse placental labyrinth development. eLife *9*, e60266. https://doi.org/10.7554/eLife.60266.

40. Gaur, P., Bielenberg, D.R., Samuel, S., Bose, D., Zhou, Y., Gray, M.J., Dallas, N.A., Fan, F., Xia, L., Lu, J., et al. (2009). Role of class 3 semaphorins and their receptors in tumor growth and angiogenesis. Clin. Cancer Res. *15*, 6763–6770. https://doi.org/10.1158/1078-0432.CCR-09-1810.

41. Milde, F., Lauw, S., Koumoutsakos, P., and Iruela-Arispe, M.L. (2013). The mouse retina in 3D: quantification of vascular growth and remodeling. Integr. Biol. (Camb) *5*, 1426–1438. https://doi.org/10.1039/C3IB40085A.

42. Oka, M., Meacham, A.M., Hamazaki, T., Rodić, N., Chang, L.J., and Terada, N. (2005). De novo DNA methyltransferases Dnmt3a and Dnmt3b primarily mediate the cytotoxic effect of 5-aza-2′-deoxycytidine. Oncogene *24*, 3091–3099. https://doi.org/10.1038/sj.onc.1208540.

43. Weedon-Fekjær, M.S., Johnsen, G.M., Anthonisen, E.H., Sugulle, M., Nebb, H.I., Duttaroy, A.K., and Staff, A.C. (2010). Expression of liver X receptors in pregnancies complicated by preeclampsia. Placenta *31*, 818–824. https://doi.org/10.1016/J.PLACENTA.2010.06.015.

44. Powers, R.W., Roberts, J.M., Plymire, D.A., Pucci, D., Datwyler, S.A., Laird, D.M., Sogin, D.C., Jeyabalan, A., Hubel, C.A., and Gandley, R.E. (2012). Low placental growth factor across pregnancy identifies a subset of women with preterm preeclampsia: type 1 versus type 2 preeclampsia? Hypertension *60*, 239–246. https://doi.org/10.1161/HYPERTENSIONAHA.112.191213.

45. Kitazawa, M., Tamura, M., Kaneko-Ishino, T., and Ishino, F. (2017). Severe damage to the placental fetal capillary network causes mid- to late fetal lethality and reduction in placental size in Peg11/Rtl1 KO mice. Genes Cells *22*, 174–188. https://doi.org/10.1111/GTC.12465.

46. Gurtner, G.C., Davis, V., Li, H., McCoy, M.J., Sharpe, A., and Cybulsky, M.I. (1995). Targeted disruption of the murine VCAM1 gene: essential role of VCAM-1 in chorioallantoic fusion and placentation. Genes Dev. *9*, 1–14. https://doi.org/10.1101/GAD.9.1.1.

47. Cift, T., Begum, A.M., Aslan Cetin, B., Erenel, H., Tuten, A., Bulut, B., Yilmaz, N., Ekmekci, H., and Gezer, A. (2020). Serum caveolin-1 levels in patients with preeclampsia. J. Matern. Fetal Neonatal Med. *33*, 712–717. https://doi.org/10.1080/14767058.2018.1500539.

48. Giussani, D.A. (2016). The fetal brain sparing response to hypoxia: physiological mechanisms. J. Physiol. *594*, 1215–1230. https://doi.org/10.1113/JP271099.

49. Tsang, J.C.H., Vong, J.S.L., Ji, L., Poon, L.C.Y., Jiang, P., Lui, K.O., Ni, Y.B., To, K.F., Cheng, Y.K.Y., Chiu, R.W.K., and Lo, Y.M.D. (2017). Integrative single-cell and cell-free plasma RNA transcriptomics elucidates placental cellular dynamics. Proc. Natl. Acad. Sci. USA *114*, E7786–E7795. https://doi.org/10.1073/pnas.1710470114.

50. Plass, C., Pfister, S.M., Lindroth, A.M., Bogatyrova, O., Claus, R., and Lichter, P. (2013). Mutations in regulators of the epigenome and their connections to global chromatin patterns in cancer. Nat. Rev. Genet. *14*, 765–780. https://doi.org/10.1038/nrg3554.

51. Wei, S.Y., and Chiu, J.J. (2021). Mechanical regulation of epigenetic modifications in vascular biology and pathobiology. Card. Vasc. Biol. *8*, 241–276. https://doi.org/10.1007/978-3-030-63164-2_9/FIGURES/3.

52. Hove, J.R., Köster, R.W., Forouhar, A.S., Acevedo-Bolton, G., Fraser, S.E., and Gharib, M. (2003). Intracardiac fluid forces are an essential epigenetic factor for embryonic cardiogenesis. Nature *421*, 172–177. https://doi.org/10.1038/nature01282.

53. Karthika, C.L., Ahalya, S., Radhakrishnan, N., Kartha, C.C., and Sumi, S. (2021). Hemodynamics mediated epigenetic regulators in the pathogenesis of vascular diseases. Mol. Cell. Biochem. *476*, 125–143. https://doi.org/10.1007/s11010-020-03890-9.

54. Lund, G., Andersson, L., Lauria, M., Lindholm, M., Fraga, M.F., Villar-Garea, A., Ballestar, E., Esteller, M., and Zaina, S. (2004). DNA methylation polymorphisms precede any histological sign of atherosclerosis in mice lacking Apolipoprotein E. J. Biol. Chem. *279*, 29147–29154. https://doi.org/10.1074/jbc.M403618200.

55. Schroeder, D.I., Blair, J.D., Lott, P., Yu, H.O.K., Hong, D., Crary, F., Ashwood, P., Walker, C., Korf, I., Robinson, W.P., et al. (2013). The human placenta methylome. Proc. Natl. Acad. Sci. USA *110*, 6037–6042. https://doi.org/10.1073/PNAS.1215145110.

56. Tekola-Ayele, F., Zeng, X., Chatterjee, S., Ouidir, M., Lesseur, C., Hao, K., Chen, J., Tesfaye, M., Marsit, C.J., Workalemahu, T., et al. (2022).

Developmental Cell
Article

CellPress
OPEN ACCESS

Placental multi-omics integration identifies candidate functional genes for birthweight. Nat. Commun. *13*, 2384. https://doi.org/10.1038/s41467-022-30007-1.

57. Zhang, B., Kim, M.Y., Elliot, G.N., Zhou, Y., Zhao, G., Li, D., Lowdon, R.F., Gormley, M., Kapidzic, M., Robinson, J.F., et al. (2021). Human placental cytotrophoblast epigenome dynamics over gestation and alterations in placental disease. Dev. Cell *56*, 1238–1252.e5. https://doi.org/10.1016/J.DEVCEL.2021.04.001.

58. Smith, Z.D., Chan, M.M., Humm, K.C., Karnik, R., Mekhoubad, S., Regev, A., Eggan, K., and Meissner, A. (2014). DNA methylation dynamics of the human preimplantation embryo. Nature *511*, 611–615. https://doi.org/10.1038/NATURE13581.

59. Guo, H., Zhu, P., Yan, L., Li, R., Hu, B., Lian, Y., Yan, J., Ren, X., Lin, S., Li, J., et al. (2014). The DNA methylation landscape of human early embryos. Nature *511*, 606–610. https://doi.org/10.1038/NATURE13544.

60. MacDonald, T.M., Walker, S.P., Hannan, N.J., Tong, S., and Kaitu'u-Lino, T.J. (2022). Clinical tools and biomarkers to predict preeclampsia. EBiomedicine *75*, 103780. https://doi.org/10.1016/J.EBIOM.2021.103780.

61. Krauss, T., Kuhn, W., Lakoma, C., and Augustin, H.G. (1997). Circulating endothelial cell adhesion molecules as diagnostic markers for the early identification of pregnant women at risk for development of preeclampsia. Am. J. Obstet. Gynecol. *177*, 443–449. https://doi.org/10.1016/S0002-9378(97)70213-8.

62. Krauss, T., Emons, G., Kuhn, W., and Augustin, H.G. (2002). Predictive value of routine circulating soluble endothelial cell adhesion molecule measurements during pregnancy. Clin. Chem. *48*, 1418–1425. https://pubmed.ncbi.nlm.nih.gov/12194917/.

63. Thadhani, R., Kisner, T., Hagmann, H., Bossung, V., Noack, S., Schaarschmidt, W., Jank, A., Kribs, A., Cornely, O.A., Kreyssig, C., et al. (2011). Pilot study of extracorporeal removal of soluble Fms-like tyrosine kinase 1 in preeclampsia. Circulation *124*, 940–950. https://doi.org/10.1161/CIRCULATIONAHA.111.034793/-/DC1.

64. Thadhani, R., Hagmann, H., Schaarschmidt, W., Roth, B., Cingoez, T., Karumanchi, S.A., Wenger, J., Lucchesi, K.J., Tamez, H., Lindner, T., et al. (2016). Removal of soluble Fms-Like tyrosine Kinase-1 by dextran sulfate apheresis in preeclampsia. J. Am. Soc. Nephrol. *27*, 903–913. https://doi.org/10.1681/ASN.2015020157.

65. De Borre, M., Che, H., Yu, Q., Lannoo, L., De Ridder, K., Vancoillie, L., Dreesen, P., Van Den Ackerveken, M., Aerden, M., Galle, E., et al. (2023). Cell-free DNA methylome analysis for early preeclampsia prediction. Nat. Med. *29*, 2206–2215. https://doi.org/10.1038/s41591-023-02510-5.

66. Herzog, E.M., Eggink, A.J., Willemsen, S.P., Slieker, R.C., Wijnands, K.P.J., Felix, J.F., Chen, J., Stubbs, A., van der Spek, P.J., van Meurs, J.B., et al. (2017). Early- and late-onset preeclampsia and the tissue-specific epigenome of the placenta and newborn. Placenta *58*, 122–132. https://doi.org/10.1016/J.PLACENTA.2017.08.070.

67. Blair, J.D., Yuen, R.K.C., Lim, B.K., McFadden, D.E., von Dadelszen, P., and Robinson, W.P. (2013). Widespread DNA hypomethylation at gene enhancer regions in placentas associated with early-onset pre-eclampsia. Mol. Hum. Reprod. *19*, 697–708. https://doi.org/10.1093/MOLEHR/GAT044.

68. Jia, R.Z., Zhang, X., Hu, P., Liu, X.M., Hua, X.D., Wang, X., and Ding, H.J. (2012). Screening for differential methylation status in human placenta in preeclampsia using a CpG island plus promoter microarray. Int. J. Mol. Med. *30*, 133–141. https://doi.org/10.3892/IJMM.2012.983.

69. Xuan, J., Jing, Z., Yuanfang, Z., Xiaoju, H., Pei, L., Guiyin, J., and Yu, Z. (2016). Comprehensive analysis of DNA methylation and gene expression of placental tissue in preeclampsia patients. Hypertens. Pregnancy *35*, 129–138. https://doi.org/10.3109/10641955.2015.1117099.

70. Chen, X., Tang, A.T., Tober, J., Yang, J., Leu, N.A., Sterling, S., Chen, M., Yang, Y., Mericko-Ishizuka, P., Speck, N.A., et al. (2022). Mouse placenta

71. fetal macrophages arise from endothelial cells outside the placenta. Dev. Cell *57*, 2652–2660.e3. https://doi.org/10.1016/J.DEVCEL.2022.11.003.

71. Cerdeira, A.S., and Karumanchi, S.A. (2012). Angiogenic factors in pre-eclampsia and related disorders. Cold Spring Harb. Perspect. Med. *2*, a006585. https://doi.org/10.1101/CSHPERSPECT.A006585.

72. Schwärzler, P., Bland, J.M., Holden, D., Campbell, S., and Ville, Y. (2004). Sex-specific antenatal reference growth charts for uncomplicated singleton pregnancies at 15–40 weeks of gestation. Ultrasound Obstet. Gynecol. *23*, 23–29. https://doi.org/10.1002/UOG.966.

73. Broere-Brown, Z.A., Baan, E., Schalekamp-Timmermans, S., Verburg, B.O., Jaddoe, V.W.V., and Steegers, E.A.P. (2016). Sex-specific differences in fetal and infant growth patterns: A prospective population-based cohort study. Biol. Sex Differ. *7*, 1–9. https://doi.org/10.1186/S13293-016-0119-1/FIGURES/3.

74. Vatten, L.J., and Skjaerven, R. (2004). Offspring sex and pregnancy outcome by length of gestation. Early Hum. Dev. *76*, 47–54. https://doi.org/10.1016/J.EARLHUMDEV.2003.10.006.

75. Liu, Y., Li, G., and Zhang, W. (2017). Effect of fetal gender on pregnancy outcomes in Northern China. J. Matern. Fetal Neonatal Med. *30*, 858–863. https://doi.org/10.1080/14767058.2016.1189527.

76. Jaskolka, D., Retnakaran, R., Zinman, B., and Kramer, C.K. (2017). Fetal sex and maternal risk of pre-eclampsia/eclampsia: a systematic review and meta-analysis. BJOG *124*, 553–560. https://doi.org/10.1111/1471-0528.14163.

77. Schalekamp-Timmermans, S., Arends, L.R., Alsaker, E., Chappell, L., Hansson, S., Harsem, N.K., Jälmby, M., Jeyabalan, A., Laivuori, H., et al.; Global Pregnancy Collaboration (2017). Fetal sex-specific differences in gestational age at delivery in pre-eclampsia: a meta-analysis. Int. J. Epidemiol. *46*, 632–642. https://doi.org/10.1093/IJE/DYW178.

78. Schindelin, J., Arganda-Carreras, I., Frise, E., Kaynig, V., Longair, M., Pietzsch, T., Preibisch, S., Rueden, C., Saalfeld, S., Schmid, B., et al. (2012). Fiji: an open-source platform for biological-image analysis. Nat. Methods *9*, 676–682. https://doi.org/10.1038/nmeth.2019.

79. Stuart, T., Butler, A., Hoffman, P., Hafemeister, C., Papalexi, E., Mauck, W.M., Hao, Y., Stoeckius, M., Smibert, P., and Satija, R. (2019). Comprehensive integration of single-cell data. Cell *177*, 1888–1902.e21. https://doi.org/10.1016/J.CELL.2019.05.031.

80. Krämer, A., Green, J., Pollard, J., and Tugendreich, S. (2014). Causal analysis approaches in Ingenuity Pathway Analysis. Bioinformatics *30*, 523–530. https://doi.org/10.1093/BIOINFORMATICS/BTT703.

81. Patro, R., Duggal, G., Love, M.I., Irizarry, R.A., and Kingsford, C. (2017). Salmon provides fast and bias-aware quantification of transcript expression. Nat. Methods *14*, 417–419. https://doi.org/10.1038/NMETH.4197.

82. Soneson, C., Love, M.I., and Robinson, M.D. (2016). Differential analyses for RNA-seq: transcript-level estimates improve gene-level inferences. F1000Research *4*, 1521. https://doi.org/10.12688/f1000research.7563.2.

83. Gu, Z., Eils, R., and Schlesner, M. (2016). Complex heatmaps reveal patterns and correlations in multidimensional genomic data. Bioinformatics *32*, 2847–2849. https://doi.org/10.1093/BIOINFORMATICS/BTW313.

84. Qiu, X., Mao, Q., Tang, Y., Wang, L., Chawla, R., Pliner, H.A., and Trapnell, C. (2017). Reversed graph embedding resolves complex single-cell trajectories. Nat. Methods *14*, 979–982. https://doi.org/10.1038/nmeth.4402.

85. Love, M.I., Huber, W., and Anders, S. (2014). Moderated estimation of fold change and dispersion for RNA-seq data with DESeq2. Genome Biol. *15*, 1–21. https://doi.org/10.1186/S13059-014-0550-8/FIGURES/9.

86. Korthauer, K., Chakraborty, S., Benjamini, Y., and Irizarry, R.A. (2019). Detection and accurate false discovery rate control of differentially methylated regions from whole genome bisulfite sequencing. Biostatistics *20*, 367–383. https://doi.org/10.1093/BIOSTATISTICS/KXY007.

87. Cavalcante, R.G., and Sartor, M.A. (2017). annotatr: genomic regions in context. Bioinformatics *33*, 2381–2383. https://doi.org/10.1093/BIOINFORMATICS/BTX183.

88. Dardik, A., Chen, L., Frattini, J., Asada, H., Aziz, F., Kudo, F.A., and Sumpio, B.E. (2005). Differential effects of orbital and laminar shear stress on endothelial cells. J. Vasc. Surg. *41*, 869–880. https://doi.org/10.1016/j.jvs.2005.01.020.

89. Hao, Y., Hao, S., Andersen-Nissen, E., Mauck, W.M., Zheng, S., Butler, A., Lee, M.J., Wilk, A.J., Darby, C., Zager, M., et al. (2021). Integrated analysis of multimodal single-cell data. Cell *184*, 3573–3587.e29. https://doi.org/10.1016/J.CELL.2021.04.048.

90. Gu, Z. (2022). Complex heatmap visualization. Imeta *1*, e43. https://doi.org/10.1002/IMT2.43.

91. Trapnell, C., Cacchiarelli, D., Grimsby, J., Pokharel, P., Li, S., Morse, M., Lennon, N.J., Livak, K.J., Mikkelsen, T.S., and Rinn, J.L. (2014). The dynamics and regulators of cell fate decisions are revealed by pseudotemporal ordering of single cells. Nat. Biotechnol. *32*, 381–386. https://doi.org/10.1038/nbt.2859.

Developmental Cell
Article

CellPress
OPEN ACCESS

STAR★METHODS

KEY RESOURCES TABLE

REAGENT or RESOURCE	SOURCE	IDENTIFIER
Antibodies		
Anti-phospho-Histone H3 (Ser10) Antibody, Mitosis Marker	Merck	#06-570
APC Rat Anti-Mouse CD31, Clone MEC 13.3 (RUO)	BD Pharmingen™	#551262; RRID: AB_398497
CD326 (EpCAM) Monoclonal Antibody (G8.8), FITC	eBioscience™	#11-5791-82; RRID: AB_11151709
Chicken anti-Rabbit IgG (H+L) Cross-Adsorbed Secondary Antibody, Alexa Fluor™ 647	Thermo Fisher Scientific	#A-21443; RRID: AB_2535861
Chicken anti-Rabbit IgG (H+L) Cross-Adsorbed Secondary Antibody, Alexa Fluor™ 488	Thermo Fisher Scientific	#A-21441; RRID: AB_2535859
Cleaved Caspase-3 (Asp175) (5A1E) Rabbit mAb	Cell Signaling	#9664
DNMT3A (D23G1) Rabbit mAb	Cell Signaling	#3598S
Donkey anti-Rabbit IgG (H+L) Highly Cross-Adsorbed Secondary Antibody, Alexa Fluor™ 546	Thermo Fisher Scientific	#A10040; RRID: AB_2534016
FITC Rat Anti-Mouse CD45, Clone 30-F11 (RUO)	BD Pharmingen™	#553080; RRID: AB_394609
FITC Rat Anti-Mouse TER-119/Erythroid Cells	BD Pharmingen™	#561032; RRID: AB_396936
FxCycle™ Violet Stain	Thermo Fisher Scientific	#F10347
Goat anti-Mouse IgG (H+L) Cross-Adsorbed Secondary Antibody, Alexa Fluor™ 488	Thermo Fisher Scientific	#A-11001; RRID: AB_2534069
Goat Anti-Rabbit Immunoglobulins/HRP	Agilent Dako	#P044801-2
Goat anti-Rat IgG (H+L) Cross-Adsorbed Secondary Antibody, Alexa Fluor™ 488	Thermo Fisher Scientific	#A-11006; RRID: AB_2534074
Hoechst 33258	Thermo Fisher Scientific	#H3569
Lectin aus Bandeiraea simplicifolia (Griffonia simplicifolia), FITC conjugate	Sigma	#L9381
Monoclonal Mouse Anti-Human CD31, Endothelial Cell (Concentrate), Clone JC70A	Agilent Dako	#M0823
Podoplanin Monoclonal Antibody (eBio8.1.1 (8.1.1)), Alexa Fluor™ 488	eBioscience™	#53-5381-82; RRID: AB_1106990
Propidium Iodide Staining Solution	eBioscience™	#00-6990-42
Purified Rat Anti-Mouse CD16/CD32 (Mouse BD Fc Block™), Clone 2.4G2 (RUO)	BD Pharmingen™	RRID: AB_394656
Purified Rat Anti-Mouse CD31, Clone MEC 13.3 (RUO)	BD Pharmingen™	RRID: AB_396660
Rabbit Anti-Human CD144	AbD Serotec	#AHP628Z
Rabbit Anti-Mouse Lyve-1	Reliatech	#103-PA50AG
Recombinant Anti-5-methylcytosine (5-mC) antibody [RM231]	abcam	#ab214727
Recombinant DNA		
GIPZ Lentiviral shRNA vector (target: *DNMT3A*; sh#1)	Horizon Discovery	#V2LHS_202509
GIPZ Lentiviral shRNA vector (target: *DNMT3A*; sh#2)	Horizon Discovery	#V3LHS_391162
GIPZ Lentiviral shRNA vector (Non-silencing Verified Negative Control; nsh)	Horizon Discovery	#RHS4346
Biological samples		
Healthy human placenta	Universitäts-Frauenklinik Heidelberg	N/A.
Chemicals, peptides, and recombinant proteins		
4-hydroxytamoxifen	Sigma Aldrich	#68047-06-3
Decitabine	Sigma Aldrich	#2353-33-5

(Continued on next page)

Continued

REAGENT or RESOURCE	SOURCE	IDENTIFIER
Puromycin	Gibco	#A1113803
Critical commercial assays		
Arcturus™ PicoPure™ RNA Isolation Kit	Thermo Fisher Scientific	#KIT0204
Click-iT™ EdU Alexa Fluor™ 488 Flow Cytometry Assay Kit	Thermo Fisher Scientific	#C10420
FITC-conjugated eBioscience™ Annexin V Apoptosis Detection Kit	Thermo Fisher Scientific	#88-8005-74
GenElute™ Mammalian Total RNA Purification Kit	Merck	#RTN70-1KT
High Sensitivity D1000 Reagents	Agilent	#5067-5585
High Sensitivity D1000 ScreenTape	Agilent	#5067-5584
Lenti-X™ Concentrator	Takara Bio Europe	#631231
Lenti-X™ Packaging Single Shots (VSV-G)	Takara Bio Europe	#631275
NEBNext® High-Fidelity 2X PCR Master Mix	NEB	#M0541L
NucleoSpin tissue mini kit for DNA from cells and tissue	Macherey-Nagel	#740952.50
Pierce™ ECL Western Blotting-Substrat	Thermo Fisher Scientific	#32106
QuantiTect Reverse Transcription Kit for cDNA Synthesis	Qiagen	#205311
Quant-iT™ dsDNA Assay Kits, high sensitivity	Thermo Fisher Scientific	#Q33120
Qubit™ RNA High Sensitivity Assay-Kit	Thermo Fisher Scientific	#Q32852
SMARTer® Universal Low Input RNA Kit for Sequencing	TaKaRa	#634940
TaqMan™ Fast Advanced Master Mix for qPCR	Thermo Fisher Scientific	#4444556
Zymo-Seq WGBS Library Kit	Zymo Research	#D5465
Deposited data		
Bulk RNA-seq of EC isolated from *Dnmt3a^fl/fl* (Cre-) versus *Dnmt3a^fl/fl*x*Cdh5-Cre* (Cre+) labyrinth ECs.	This study	GSE280085
Human placenta single-cell RNA-seq data (raw data)	Tsang et al.[49]	N/A
Mouse labyrinth EC single-cell RNA-seq	This study	GSE280168
Mouse placenta Seurat object	Marsh and Blelloch[39]	Processed R object: https://figshare.com/projects/Single_nuclei_RNA-seq_of_mouse_placental_labyrinth_development/92354
WGBS of EC isolated from *Dnmt3a^fl/fl* (Cre-) versus *Dnmt3a^fl/fl*x*Cdh5-Cre* (Cre+) labyrinth ECs.	This study	GSE280086
Experimental models: Cell lines		
Human: JEG3	ATCC	#HTB-36
Human: Lenti-X™ 293T Cell Line	Takara Bio Europe	#632180
Human: Pooled donors HUVEC	Promo Cell	#C-12253
Experimental models: Organisms/strains		
Mouse: B6(Cg)-Dnmt3a^tm1b(KOMP)Wtsi	Jackson Laboratory	No. 018838
Mouse: C57BL/6 *Dnmt3a^flox/flox* mice	RIKEN BioResource Center	No. RBRC03731
Mouse: C57BL/6 *Cdh5*-Cre mice (*B6;129-Tg(Cdh5-cre)1Spe/J*)	Jackson Laboratory	RRID: IMSR_JAX:017968
Mouse: C57BL/6 *Cdh5*-Cre^ERT2 mice (*Tg(Cdh5-cre/ERT2)1Rha*)	Kindly provided by Dr. Ralf Adams, MPI, Münster, Germany	N/A
Mouse: C57BL/6NRj	Janvier Labs	N/A
Oligonucleotides		
Genotyping primer *Actb* fwd: CAATGGT AGGCTCACTCTGGGAGATGATA	eurofins	N/A
Genotyping primer *Actb* rev: AACACAC ACTGGCAGGACTGGCTAGG	eurofins	N/A
Genotyping primer Cre fwd: GCCTGCA TTACCGGTCGATGCAACGA	eurofins	N/A

(Continued on next page)

Developmental Cell
Article

CellPress
OPEN ACCESS

Continued

REAGENT or RESOURCE	SOURCE	IDENTIFIER
Genotyping primer Cre rev: GTGGCAG ATGGCGCGGCAACACCATT	eurofins	N/A
Genotyping primer *Dnmt3a*^fl/fl fwd: CTGGT GATTGGAGGCAGTCCATGCA	eurofins	N/A
Genotyping primer *Dnmt3a*^fl/fl rev: TAGCT GAGGCTGTCTGCATCGGACA	eurofins	N/A
Genotyping primer *Dnmt3a*^+/+ fwd: ACAAC AGTTTCTCCCTGTGAC	eurofins	N/A
Genotyping primer *Dnmt3a*^+/+ rev: CAATG AAGAGTGGGTGCTC	eurofins	N/A
Genotyping primer *Dnmt3a*^−/− fwd: CGCTA CCATTACCAGTTGGTC	eurofins	N/A
Genotyping primer *Dnmt3a*^−/− rev: GCTCAT CACCCTGAGATGCC	eurofins	N/A
Software and algorithms		
Fiji	Schindelin et al.[78]	https://fiji.sc/
Graphpad Prism (v8.0)	GraphPad Software.	https://www.graphpad.com
Seurat	Stuart et al.[79]	https://github.com/satijalab/seurat
EnhancedVolcano	–	https://github.com/kevinblighe/ EnhancedVolcano
QIAGEN Ingenuity Pathway Analysis	Krämer et al.[80]	N/A
bcl2fastq (v2.20.0.422)	Illumina	N/A
Salmon	Patro et al.[81]	https://biocorecrg.github.io/RNAseq_ course_2019/salmon.html
tximport	Soneson et al.[82]	N/A
pheatmap	Gu et al.[83]	N/A
SeuratWrapper	–	https://github.com/satijalab/ seurat-wrappers
Monocle 3	Qiu et al.[84]	https://cole-trapnell-lab.github.io/ monocle3/
DESeq2	Love et al.[85]	N/A
dmrseq	Korthauer et al.[86]	N/A
annotatr	Cavalcante et al.[87]	N/A
R	r-project.org	https://www.r-project.org/
Other		
AMPure XP	Beckman Coulter	#A63881
Collagen from rat tails	Self-produced	N/A
Fluorescence Mounting Medium	Agilent Dako	#S302380-2
Tissue-Tek® O.C.T. Compound	Sakura	#4583

EXPERIMENTAL MODEL AND STUDY PARTICIPANT DETAILS

Mice

Mice were housed in individually ventilated cages under pathogen-free conditions. Animals had free access to food and water and were kept in a 12h light-dark cycle. All mice were handled according to the German national guidelines and as approved by the regional council Karlsruhe (G-82/19, G-283/18, G-83/23, DKFZ370). Heterozygous *Dnmt3a* knockout mice (B6(Cg)-Dnmt3a^tm1b(KOMP)Wtsi) were obtained from Jackson Laboratory (# No. 018838) to generate homozygous *Dnmt3a* knockout mice. C57BL/6 *Dnmt3a*^fl/fl mice (RIKEN BioResource Center, No. RBRC03731) were crossed with C57BL/6 *Cdh5*-Cre mice (*B6;129-Tg(Cdh5-cre)1Spe/J*; Jackson Laboratory). For postnatal *Dnmt3a* deletion, C57BL/6 *Dnmt3a*^fl/fl mice were crossed with C57BL/6 *Cdh5-Cre*^ERT2 mice (*Tg(Cdh5-cre/ERT2)1Rha*; kindly provided by Dr. Ralf Adams, MPI, Münster, Germany) to specifically delete *Dnmt3a* in *Cdh5*-expressing cells upon 4-Hydroxytamoxifen application. Cre-negative mice, equally treated with 4-Hydroxytamoxifen, were used as controls. Pups were intragastrically injected with three doses of 4-Hydroxytamoxifen (50µg) (Sigma) at P2, P3, and P5 dissolved in ethanol and corn oil.

Human sample collection

Human full-term placenta samples that were considered to have normal placentation, were collected immediately after resection. Tissue was dissected from the fetal side of the placenta and embedded in O.C.T. Human material collection was approved by the local ethics committee (S-320/2022). Informed consent was obtained from all participants for the use of human tissues in research, in compliance with ethical guidelines and approved institutional protocols.

METHOD DETAILS

EC isolation by FACS

To sort placenta ECs, the isolated placentas were cut in the sagittal plane. From each half, the decidua was removed with a microscissor without disturbing the labyrinth. Labyrinth and decidua samples were digested with DNAseI (Roche, 20U/ml)/Liberase (Liberase TM Research Grade, Merck, 1.3U/ml) in DMEM (Gibco) for 15min at 37°C. After the tissue was gently disintegrated by passing the mixture through an 18-G needle, the samples were incubated for another 15min at 37°C. The cell suspension was passed through a 100μm cell strainer. Erythrocyte lysis was performed by resuspending the cell pellet in ACK buffer following an incubation for 5min at RT. To block non-specific binding, samples were incubated with anti-mouse CD16/32 antibody (Purified Rat Anti-Mouse CD16/CD32, Clone 2.4G2 (RUO), BD Pharmingen, RRID: AB_394656, 1:100). Cells were washed and incubated with the antibody staining mix (Purified Rat Anti-Mouse CD31, Clone MEC 13.3 (RUO), BD Pharmingen, RRID: AB_396660, 1:100; FITC Rat Anti-Mouse TER-119/Erythroid Cells, BD Pharmingen, #561032, RRID: AB_396936, 1:200; Podoplanin Monoclonal Antibody (eBio8.1.1 (8.1.1)), Alexa Fluor 488 eBioscience, #53-5381-82, RRID: AB_1106990; 1:100; CD326 (EpCAM) Monoclonal Antibody (G8.8), FITC, eBioscience™, #11-5791-82, RRID: AB_11151709, 1:200; FITC Rat Anti-Mouse CD45, Clone 30-F11 (RUO), BD Pharmingen, #553080, RRID: AB_394609, 1:400), before sorting the samples. Dead cells were excluded by propidium iodide (Propidium Iodide Staining Solution, eBioscience™, #00-6990-42, 1:20,000) staining. Live CD45⁻/CD326⁻/Pdpn⁻/Ter119⁻/CD31⁺ cells were sorted with a BD FACSAria ll (BD Biosciences) for bulk samples. For the placenta labyrinth EC sort, a FACSAria III (BD Biosciences) was used.

Whole genome bisulfite sequencing (WGBS)

WGBS library preparation was performed from FACS-sorted placenta ECs from litter-matched $Dnmt3a^{flox/flox}$ $xCdh5$-Cre and $Dnmt3a^{flox/flox}$ embryos in triplicates. Therefore, DNA was isolated using the QIAmp DNA Micro kit (Qiagen) according to manufacturer instructions. DNA was eluted in water and the concentration was measured using the Qubit dsDNA HS Assay (Thermo Fisher Scientific) with the Qubit 3.0 fluorometer (Thermo Fisher Scientific). For the bisulfite library preparation, the Zymo-Seq WGBS library kit (Zymo Research) was used and library validation and quantification were done with the High Sensitivity D1000 ScreenTape (Agilent Technologies) and analyzed with the TapeStation Analysis Software 4.1 (Agilent Technologies). Libraries were equimolar pooled and the resulting multiplex was sequenced on a NovaSeq 6000 using the S4 100 cycle paired-end kit in the DKFZ NGS core facility.

Singel-cell library generation and sequencing

Whole transcriptome scRNA-seq was performed following an adapted SMARTseq2.5 protocol. For each sample, single cells were sorted in 384-well plates into 1μl of lysis buffer containing RNase inhibitors and a biotinylated polyT oligo. RNA was extracted using streptavidin beads with the Agilent Bravo system. For the reserve transcription reaction, a TSO with LNAs (Eurogentec) at a final concentration of 3μM and the Maxima H Minus reverse transcriptase (Thermo) under molecular crowding conditions with 7.5% PEG-8000 were used. Subsequently, PCR was performed with the KAPA HiFi HotStart ReadyMix (KAPA Biosystems) and an IS PCR primer (ISPCR) on a thermal cycler using the following protocol: 98°C for 3min, followed by 16 cycles of 98°C for 20s, 67°C for 15s, 72°C for 6min, followed by a final 5min extension at 72°C. Samples were purified with AMPure XP beads (Beckman) at a 0.7x ratio using the Agilent Bravo system. Library preparation was done via Tn5 tagmentation using 1ng as input per cell. Tagmentation was stopped with SDS (0.02% final concentration). Libraries were amplified using Nextera indices (Sigma), KAPA HiFi HotStart ReadyMix (KAPA Biosystems), and 0.05% DMSO. Pipetting steps were done with the mosquito LV (SPTlabtech) and the Mantis system (Formulatrix). After pooling all libraries from one plate, quantification and quality control using the Qubit fluorometric quantification (ThermoFisher Scientific) and TapeStation system (Agilent) was performed, and the cDNA libraries were sequenced on a NovaSeq 6000.

RNA-sequencing

For bulk RNA-seq, RNA was isolated from FACS-sorted labyrinth placenta ECs from $Dnmt3a^{flox/flox}$ $xCdh5$-Cre and $Dnmt3a^{flox/flox}$ embryos in triplicates using the Arcturus PicoPure RNA Isolation Kit (Thermo Fisher Scientific) according to manufacturer instructions. Libraries were generated by the NGS core facility of the DKFZ using the SMARTer Ultra-low RNA kit (Takara), multiplexed oligos for Illumina (NEBNext), and the High Fidelity 2x PCR master mix (NEBNext). Libraries were equal molar pooled and the resulting multiplex was sequenced on a NexSeq 550 using the 75bp high-output cycle single-end kit in the DKFZ NGS core facility.

Developmental Cell
Article

CellPress
OPEN ACCESS

RNA isolation, reverse transcription, and quantitative measurement

For qPCRs, snap frozen tissue was mechanically disrupted with 5mm sized metal beads in TRI Reagent (Sigma, T9424), following RNA extraction using phenol:chloroform. Samples from cell culture were harvested in the RNA extraction buffer supplemented with 10mM ß-ME. RNA was purified using the GenElute Mammalian total RNA Miniprep kit (Merck) according to manufacturer instruction. Reverse transcription was performed using the QuantiTect Reverse Transcription Kit (Qiagen) according to the manufacturer's instructions. TaqMan Fast Advanced Mastermix (Thermo Fisher Scientific) was used to detect mRNA transcription levels. Reactions were performed in 384-well format on the StepOnePlus Real-Time PCR system. The used TaqMan gene expression assays were purchased from Thermo Fisher Scientific. The following TaqMan gene expression assays were used for murine samples: Mm00607939_S1 (*Actb*), Mm00483057_m1 (*Cav1*), Mm03053893_gH (*Ccnb1*), Mm01171453_m1 (*Ccnb2*), Mm00432359_m1 (*Ccnd1*), Mm01135198_m1 (*Cd36*), Mm01151063_m1 (*Dnmt1*), Mm00432881_m1 (*Dnmt3a*), Mm01240113_m1 (*Dnmt3b*), Mm00475056_m1 (*Lyve1*), Mm01278617_m1 (*Mki67*), Mm00448100_g1 (*Pcna*), Mm01242584_m1 (*Pecam1/Cd31*), Mm00435613_m1 (*Pgf*), Mm00477872_m1 (*Uhrf1*) and Mm01320970_m1 (*Vecam1*).

The following TaqMan gene expression assays were used for human samples: Hs00962877_m1 (*ACP1*), Hs01060665_g1 (*ACTB*), Hs00969450_g1 (*ADM*), Hs05001325_s1 (*AMIGO2*), Hs01048042_m1 (*ANGPT2*), Hs00270873_s1 (*APLNR*), Hs01582072_m1 (*AURKA*), Hs00945858_g1 (*AURKB*), Hs00186432_m1 (*CDC14A*), Hs00372920_m1 (*CDC14B*), Hs00426680_mH (*CDC20*), Hs00355782_m1 (*CDKN1A*), Hs00183740_m1 (*DKK1*), Hs00184092_m1 (*DLL4*), Hs00945875_m1 (*DNMT1*), Hs01027162_m1 (*DNMT3A*), Hs00171876_m1 (*DNMT3B*), Hs01107363_gH (*ETF1*), Hs00852949_g1 (*HMGA1*), Hs00607129_gH (*HSPA5*), Hs00360439_g1 (*KLF2*), Hs00272659_m1 (*LYVE1*), Hs04260396_g1 (*MKI67*), Hs00427214_g1 (*PCNA*), Hs00182176_m1 (*PGF*), Hs01597839_m1 (*PRC1*), Hs00377726_m1 (*PTGS1*), Hs00178579_m1 (*SMAD6*) and Hs00900710_m1 (*UNC5B*).

Retina angiogenesis assay

The eyeballs of P7 pups were fixed in ice-cold methanol at -20°C. Blocking and permeabilization of the isolated retinas were performed with 10% normal goat serum/ 0.5% Triton-X 100/ 1% BSA in PBS. The retinal vasculature was stained by incubation with isolectin B4 (Lectin from Bandeiraea simplicifolia (Griffonia simplicifolia), FITC conjugate, Sigma, #L9381, 1:100) and the primary antibody (Anti-phospho-Histone H3 (Ser10) Antibody, Mitosis Marker, Merck, #06-570, 1:200) diluted in 0.2% Tween-20/ 1% BSA in PBS, followed by incubation with secondary antibody. Fluorescently labeled retinas were flat-mounted with DAKO mounting medium on microscope slides and imaged using the confocal Zeiss LSM710 microscope with a 20x/0.4 Dry objective. Image analysis was done in ImageJ. The vascularized area was normalized to the whole retina area. All values were normalized to the average of the littermate WT animals.

Histology

For immunofluorescent staining, Tissue-Tek O.C.T. embedded cryopreserved tissue was cut into 7μm sections and fixed in ice-cold methanol. For immunohistochemical stainings, paraffin-embedded tissue was cut and sections were rehydrated, following antigen retrieval with citrate buffer. Blocking and tissue permeabilization was performed in 10% normal donkey serum/ 3% BSA, followed by incubation with the appropriate primary antibodies (Anti-Mouse CD31, BD Pharmingen, RRID: AB_396660, 1:100; Anti-Human CD31, Agilent Dako, #M0823, 1:200; Anti-DNMT3A, Cell Signaling, #3598S, 1:100; Anti-Mouse Lyve-1, Reliatech, #103-PA50AG, 1:200; Cleaved caspase-3 (Asp175) (5A1E) Rabbit mAb, Cell Signaling, #9664, 1:150; Rabbit Anti-Human CD144, AbD Serotec, #AHP628Z, 1:100). After washing with TBST, sections were incubated with appropriate secondary antibodies. Hoechst 33258 was used for nuclei visualization. Slides were mounted using DAKO mounting medium and images were taken with the Zeiss Axio Scan.Z1 using an air 20×/ 0.8 Plan-APOCHROMAT objective. Image analysis was done in ImageJ.

Cell culture and *in vitro* studies

HUVECs (C-12253) were purchased from PromoCell and cultured in Endopan 3 supplemented with 3% FCS and supplements (PAN Biotech) at 37°C, 5% CO_2 and high humidity maximum until passage 6. Cell culture plates were coated with 0.1% gelatin prior to cell seeding. For manipulation of flow conditions *in vitro*,[88] HUVECs were placed in a temperature-controlled orbital shaker (Edmund Buehler) set to 37°C. To mimic flow, cells were shaken at 200rpm with a shear of 14dyne/cm^2 for 24h. For the DNA de-methylation study, HUVECs were treated with 500nM Decitabine (Sigma Aldrich) dissolved in 0.9% NaCl or with an equal volume of 0.9% NaCl as control. Cells were passaged two times before harvesting. The media was changed every day. Prior to cell proliferation analysis, HUVECs were starved in medium without supplements for 1h. EdU was added at a final concentration of 10μM for 3h. Harvesting, fixation, permeabilization, and staining were performed using the Click-iT EdU Flow Cytometry Assay Kit Alexa Fluor 488 (Thermo Fisher Scientific) according to the manufacturer's protocol. Annexin V assay was performed using the FITC conjugated eBioscience Annexin V Apoptosis Detection kit (Thermo Fisher Scientific) according to the manufacturer's protocol. FxCycle Violet stain was used instead of PI. Cells were analyzed on a BD FACSCanto II (BD Bioscience). For knockdown experiments upon lentiviral transduction with GIPZ-shRNA encoding virus (nsh: Non-silencing Verified Negative Control, #RHS4346; sh#1: shRNA against *DNMT3A*, #V2LHS_202509; sh#2: shRNA against *DNMT3A*, V3LHS_391162), cells were selected with puromycin (0.4 μg/ml) for 4–6 days.

JEG3 (HTB-36) were purchased from ATCC and cultured in EMEM supplemented with 2mM L-glutamine, 1% Non-Essential Amino Acids, 1mM sodium pyruvate (CLS), 10% FCS, and 1% Penicillin Streptomycin Solution at 37°C, 5% CO_2 and high humidity. Upon lentiviral transduction with GIPZ-shRNA encoding virus, cells were selected with puromycin (0.4 μg/ml) for 4-6 days.

DNA methylation analysis via dot blot

Genomic DNA was isolated using the NucleoSpin Tissue-Mini kit for DNA from cells and tissue (Macherey-Nagel). Genomic DNA was sheared with a 30-G syringe. DNA was mixed with 20µl denaturation buffer (1M NaOH, 25mM EDTA) and boiled for 10min at 95°C. Samples were placed on ice and mixed with 50µl neutralization buffer (2M ammonium acetate, pH 7.0). Nitrocellulose membranes were fixed in a microfiltration blotting device (Bio Dot Apparatus). DNA was applied and membranes were washed and air-dried following UV-crosslinking. After blocking with 5% milk in TBS-T for 1h at RT, incubation with the primary antibody Recombinant Anti-5-methylcytosine (5-mC antibody [RM231], abcam, #ab214727, 1:500) was performed at 4°C overnight. After washing, the membrane was incubated with HRP-conjugated secondary antibody (Goat Anti-Rabbit Immunoglobulins/HRP, Agilent Dako, #P044801-2, 1:5,000) for 1h at RT. After washing, membranes were developed with ECL solution (Thermo Scientific Pierce) and images were acquired using an Amersham imager 600 (GE Healthcare).

QUANTIFICATION AND STATISTICAL ANALYSIS

Quantification of vessel parameters in the murine placenta

To evaluate the labyrinth vascularization, the vascular outgrowth in the sagittal plane was quantified based on the CD31 staining (pan-EC marker). The labyrinth outgrowth was measured from the bottom to the upper edge of the labyrinth at three defined positions (the chorionic plate was not included in the measurement). Initially, measurements were taken at the midpoint of the labyrinth. Subsequently, measurements were taken at equal distances from the midpoint towards the left and right sides of the labyrinth. The average outgrowth, derived from these three measurements, was then normalized to litter-matched samples to ensure accurate comparisons across samples.

To analyze the vascular density, vessel lumen, and extravascular space, images were processed automatically, using in-house developed Fiji macro. In short, images were background subtracted, median filtered and an automatic threshold with Li method was applied to convert images to masks. The masks were further processed with the skeleton tool and distance mapping was applied to measure the thickness of the lumen and empty space. The area fraction was measured using ROI (region of interest) Manager Measure tool for the selected regions of interest. Data was normalized to litter-averaged Cre⁻ samples.

Quantitative PCR analysis

Differences in the mRNA levels detected using the TaqMan Fast Advanced Mastermix (Thermo Fisher Scientific) were assessed with the Ct-method. Therefore, the Ct value of each gene of interest was normalized to the respective Ct value of *Actb* for each sample. The resulting ΔCt values were used to calculate relative gene expression. Precisely, ΔCt-values for individual samples were normalized to the average ΔCt of all control samples. The resulting ΔΔCt values were then used to calculate the relative fold change as $2^{-\Delta\Delta Ct}$.

Quantification of global DNA methylation changes assessed via dot blot

Chemiluminescent signal analysis was performed using Fiji. The integrated density for each sample (dot) was measured, and the values were normalized to the amount of input DNA applied per sample.

Human single-cell data analysis

The human placenta single-cell RNA sequencing data were provided on request from Tsang et al..[49] Data was analyzed in R using the package Seurat.[79,89] Cells with fewer than 200 or greater than 2500 unique genes and with greater than 5% mitochondrial counts, were excluded from analyses. For the analysis of normal placenta cells, individual healthy placenta samples were merged and counts were scaled and log₂-normalized using ScaleData and NormalizeData, respectively. PCA was performed with the 2,000 most highly variable features (assessed with FindVariableFeatures as input). Significant dimensions were assessed using ElbowPlot and clustering was performed using 15 dimensions and a resolution of 0.3 with FindNeighbors and FindClusters, respectively. Genes for cluster annotation were extracted from Tsang et al.[49]. Maternal decidua cells were annotated based on *DKK1*, *IGFBP1*, *VEGFA,* and *F2R* expression. Maternal uterine dendritic cells were annotated based on *CD52*, *CD83*, *CD86,* and *TREM2* expression. Villous stromal cells were annotated based on *ECM1*, *FIBIN*, *HGF,* and *BMP5* expression. Hofbauer cells were annotated based on *CD163*, *CD209*, *STAB1,* and *CD14* expression. Vascular smooth muscle cells were annotated based on *CNN1*, *MYH11*, *AOC3,* and *LMOD1* expression. Monocytes were annotated based on *CSF1R*, *CD53*, *AIF1,* and *CD14* expression. Extravillous trophoblast cells were annotated based on *MMP11*, *PAPPA2*, *HLA-G,* and *AIF1L* expression. Endothelial cells were annotated based on *CDH5*, *CD34*, *PLVAP,* and *VWF* expression. Subsyncytial cytotrophoblast cells were annotated based on *CGA*, *CYP19A1*, *GH2,* and *FAR2* expression. Villous cytotrophoblast cells were annotated based on *PARP1*, *FOXO4*, *FAM3B,* and *DNMT1* expression.

To assess the log₂-normalized expression of epigenetic modifiers in the defined cell populations, gene lists for "chromatin remodeling", "histone modification" and "DNAme alteration" were defined[50] (Table S1). The "DNAme alteration" signature was further separated into "writer", including *DNMT1*, *DNMT3A,* and *DNMT3B*, and "editor" including *TET1*, *TET2,* and *TET3*. The expression scores for the defined gene lists were added using AddModuleScore. Data were visualized with DotPlot. The expression of individual genes was also generated with the DotPlot function. To extract ECs from healthy and diseased placentas, an EC score was assigned to each cell based on the expression of manually curated key EC genes (*CD34*, *CDH5*, *ERG*, *TIE1*, *TEK,* and *VWF*) using AddModuleScore. Cells with an EC score higher than 0.4 were selected as a subset for further analysis. ECs from healthy and

Developmental Cell
Article

CellPress
OPEN ACCESS

diseased placentas were merged with Merge. Clustering was performed as described above with a dimension of 9 and a resolution of 0.5. DimPlot was used to show the EC score expression in the extracted ECs and their health state. The differential gene expression analysis on extracted ECs was performed based on their health state (healthy vs. diseased) using the Wilcoxon Rank Sum test. Differentially expressed genes were assessed with FindAllMarkers. Only genes that were detected in a minimum fraction of 10% of cells and passed the threshold of 0.25 fold change were used. Data were visualized as a volcano plot with EnhancedVolcano (version 1.8.0). Functional gene annotation was performed through the use of QIAGEN Ingenuity Pathway Analysis.[80]

Murine placenta single-cell data analysis
The mouse placenta Seurat object was obtained from Marsh and Blelloch.[39] The package Seurat[79,89] was used for data analysis. Cells with fewer than 600 or greater than 3,000 unique genes and with greater than 12% mitochondrial transcripts were excluded from the following analysis. PCA was performed using RunPCA with the 2000 most highly variable features (assessed with FindVariableFeatures) as input. Clustering was performed using 17 dimensions and a resolution of 0.5 with FindNeighbors and FindClusters, respectively. To extract ECs, a manually curated EC score was assigned to each cell based on the expression of key EC genes (*Pecam1*, *Erg*, *Tie1*, *Tek,* and *Kdr*). Cells with an EC score higher than 0.75 were used for further analysis. The data were $\log_2$-normalized and scaled with NormalizeData and ScaleData, respectively, and further processed as described above. For cell clustering, 13 dimensions with a resolution of 0.5 were used. To distinguish between maternal and fetal ECs, that dataset was reduced to male placenta samples (E12.5 and E14.5). Discrimination of maternal and fetal ECs was assessed based on *Xist* expression. The dataset contained ECs with either low (n=890, male) or high (n=58, female) *Xist* expression (Figure S2D). The difference in the number of gender-specific cells was due to the selective enrichment for the labyrinth layer. The expression of epigenetic modifiers was assessed as described above. Data visualization was performed using the DotPlot, DoHeatmap, and VlnPlot functions.

Murine labyrinth EC single-cell data analysis
Raw sequencing data were demultiplexed and FASTQ files were generated using bcl2fastq software (Illumina, v2.20.0.422). Using salmon,[81] FASTQ files were mapped to the GRCm39 mouse reference genome and count matrices were constructed with the R package tximport.[82] Resulting count matrices were log normalised and analysed using the R package Seurat.[79,89] Read count per cell, gene count per cell and the percentage of mitochondrial transcripts were computed using the respective functions in the Seurat package. ECs with fewer than 1,500 or greater than 7,500 unique genes and with greater than 5% mitochondrial transcripts were excluded from the following analysis. Gene counts were scaled and $\log_2$-normalized using ScaleData and NormalizeData, respectively. PCA was performed using RunPCA with the 2000 most highly variable features (assessed with FindVariableFeatures) as input. Clustering was performed using 20 dimensions and a resolution of 1 with FindNeighbors and FindClusters, respectively. The top 10 marker genes for the identified clusters based on the average $\log_2$ fold change was extracted and visualized using the R package pheatmap.[83,90] Trajectory analysis of placenta ECs was performed using the R packages SeuratWrapper and Monocle 3.[84,91] First, the generated Seurat object was converted to a CellDataSet object using the function as.cell_data_set from the package SeuratWrappers. Then, the pseudotime trajectory was build based on selected root nodes in cluster 2 using the function order_cells from the R package Monocle 3. The calculated trajectory colored by pseudotime was plotted with plot_cells. The calculated pseudotime values were added to the initial Seurat object. Scatterplots were generated using the function FeatureScatter from the Seurat package. A polynominal regression curve was plotted using geom_smooth(method="lm"). Gene scores for flow responsive gene sets (flow induced or flow repressed) for each cell were calculated using the AddModuleScore function in Seurat. The following genes were used for the flow-induced gene expression score: *Klf4, Atf3, Hspa1b, Jun, Xbp1, Hspa1a, Hspa5, Dusp1, Nfil3, Map3k3, Nr4a1, Nos3, Wnt9b, Fos, Arc, Dnajb1, Cks2, Ier5l, Hspa8,* and *Hsp90aa1*. The following genes were used for the flow-repressed gene expression score: *Fam43a, Angpt2, Camk2g, Camk2b, Camk2d, Edn1, Sema7a, Cxcr4, Pde4b, Ier3, Dusp6, Klf6, Sgk1, Ccdc71, Arrdc3, Gprin3, Snrk, Rhob, Kit,* and *Id3*.

RNA-seq analysis
Prior to analysis, genes count matrix was filtered to include genes with minimum total 5 raw counts across samples. Differential gene expression analysis was performed using the DESeq2 package.[85] Sex of the samples was estimated based on the percentage of coverage of Y-chromosome reads in each sample (number of reads in chromosome Y/total number of reads in each sample). Sex chromosomes were included in the RNA-seq data analysis. For each group individually, pairwise Wald tests between conditions Cre^+ against Cre^- EC were performed. Significant differentially expressed genes were defined using the following thresholds: Benjamini-Hochberg-adjusted p-value<0.05. For visualizations, clustered heatmaps were generated clustering both samples (columns) and differentially expressed genes (rows) using Euclidean distance and 'Ward.D' clustering method. Volcanoes were also generated highlighting differentially expressed genes where downregulated are annotated in blue and upregulated in red. Top 3 differentially expressed genes from either direction (up or down) are labelled with their corresponding gene symbols.

WSBS analysis
Differentially methylated regions were identified using the Bioconductor package dmrseq[86] (CpGs per region $\geq$ 5; max. distance between CpGs: 1kb). Genomic feature annotation was done using the Bioconductor package annotatr.[87] Sex of the samples was estimated based on the percentage of coverage of Y-chromosome reads in each sample (number of reads in chromosome Y/total number of reads in each sample). Sex chromosomes were removed from DNA methylation during the filtering process, before differential

Developmental Cell
Article

methylation analysis. For the association of DEGs (adj. *p*-value<0.05; log$_2$FC>1) with DMRs (FDR<0.05), directly with the DEG overlapping DMRs were kept and used for visualization. A linear regression line was plotted using geom_smooth(method="lm").

Statistical analysis

Statistical analyses were performed using GraphPad Prism version 8 and R. Data are expressed as mean ± SD. A p-value of <0.05 was considered statistically significant and marked by asterisks (*p<0.05, **p<0.01, ***p<0.001, ****p<0.0001). The performed statistical tests are specified in the figure legends. Unless otherwise stated, n represents the number of independent mice or samples in biological replicates analyzed per group or condition. Detailed information is provided in the figure legends.